2005

High Resistivity Zinc Stannate As A Buffer Layer In CdS/CdTe Solar Cells

Sudhakar R. Gayam
University of South Florida

High Resistivity Zinc Stannate As A Buffer Layer In CdS/CdTe Solar Cells

by

Sudhakar R. Gayam

A thesis submitted in partial fulfillment
of the requirements for the degree of
Master of Science in Electrical Engineering
Department of Electrical Engineering
College of Engineering
University of South Florida

Major Professor: Christos S. Ferekides, Ph.D.
Don L. Morel, Ph.D.
Yun L. Chiou, Ph.D.

Date of Approval:
March 23, 2005

Keywords: semiconductors, thin films, transparent conducting materials, sputtering, interdiffusion

ACKNOWLEDGEMENTS

I would like to thank my Major Professor, Dr. Chris Ferekides, for giving the opportunity to work towards my Master's Thesis. I am very grateful to him for having providing me the inspiration to learn and explore all the areas that fall under our research group. I would like to thank Dr. Don Morel for his feedback during our group meetings. I would also like to thank Dr. Y.L.Chiou for agreeing to be in my committee.

I would like to thank Dr. Robert Mamazza for helping me get started in our group. I would like to thank my colleagues Zhao, Srilatha, Lin, Mathesh, Swetha, Venkat, Vikram and Prashant for being very supportive and co-operative all through my research. Last but not least, I would like to thank my family who has been the pillar of support during each and every phase of my educational career.

DEDICATION

This thesis is dedicated to the cherished memory of my mother

TABLE OF CONTENTS

LIST OF TABLES

LIST OF FIGURES

HIGH RESISTIVITY ZINC STANNATE AS A BUFFER LAYER IN CdS/CdTe SOLAR CELLS

Sudhakar R. Gayam

ABSTRACT

The electrical conductivity of transparent conducting oxides is well exploited in front surface electrodes for solar cells where high transmission is also important. Fluorine doped tin oxide (SnO_2: F) is the most popular choice of front contacts for CdTe solar cells. In this thesis, Cd_2SnO_4 and Zn_2SnO_4 thin films are investigated focusing on their electrical and optical properties and used them in solar cells. Processing for these materials is optimized for optimum solar cell performance.

Cd_2SnO_4 thin films are deposited by co-sputtering of CdO and SnO_2 targets in Ar ambient at room temperature. Then films are subjected to high temperature annealing in He ambient. The films crystallize in inverse spinel structure. The average transmission of a Cd_2SnO_4 thin film with a thickness of 2500Å obtained in this study is 92%. The lowest resistivity obtained in this work for a Cd_2SnO_4 film with a thickness of 2500Å is 5.4 X 10^{-4} Ω-cm. The effect of stoichiometry on structure, optical and electrical properties of Cd_2SnO_4 is studied by varying the amount of CdO and SnO_2 in the Cd_2SnO_4 film.

Zinc stannate thin films are deposited by co-sputtering of ZnO and SnO_2 targets in Ar ambient at both room temperature and elevated temperatures. As deposited and high temperature annealed Zn_2SnO_4 thin films are highly resistive. The average transmission

of a Zn_2SnO_4 thin film with a thickness of 2000Å and annealed at 600°C in He has been 94%. Zn_2SnO_4 thin films are incorporated as a buffer layers into CdTe solar cells.

SnO_2: F is used as a front contact in CdTe solar cells in conjunction with high resistive Zn_2SnO_4 buffer layer.

The best SnO_2:F /zinc stannate cell device performance for room temperature deposited zinc stannate film resulted for the device with Zn/Sn =2.1. It has an efficiency of 12.43% with V_{OC} = 810mV, FF = 66.6% and J_{SC} = 23.1 mA. The best SnO_2:F /zinc stannate cell device performance for Zn_2SnO_4 thin film deposited at 400°C resulted for the device with 500Å thick zinc stannate. It has an efficiency of 14.21% with V_{OC} = 830mV, FF = 69.3% and J_{SC} = 24.74 mA.

CHAPTER 1

INTRODUCTION

The energy demand is ever increasing with time but the availability of energy resources is depleting day-by-day. Most of the energy that we use today comes from fossil fuels like coal, petroleum and natural gas. With the sudden rise in the energy needs, we have already consumed a major percentage of these fossil fuels, which are nonrenewable and exhaustible. Acute shortage will occur in the very near future. Moreover the combustion of fossil fuels is the primary concern. It causes air pollution which is not only dangerous to human health but also causes an imbalance among the gases present in the earth's atmosphere. Combustion increases the concentration of carbon dioxide which is the main reason for global warming.

1.1 Different forms of energy

Growing concern over the availability of fossil fuels drives mankind in search of viable alternatives like nuclear fission, nuclear fusion, wind, hydroelectric, solar etc. Nuclear power generation encounters problems with the disposal of radioactive waste and the maintenance of nuclear reactors. Electrical power generation by wind is unreliable and economically not feasible. Most non controversial way of generating electricity is hydroelectric power but it accounts for only a small percentage of the energy needed. T

able 1 gives the survey of various energy sources with the advantages and disadvantages associated with them [24]. Compared to various energy sources, solar energy has several advantages. The source of solar energy (Sun) is unlimited for all purposes. Solar cells cause no harm to the environment. Solar power generation is also versatile; it can be done on a large scale as well as on a small scale. Solar cells are also of great use in space applications. In order for solar cells to be available for commercial use, they have to overcome two important challenges: cost and storage. The cost of solar power must be competitive to the cost of power generated by the present day generation schemes. This can be accomplished by increasing the efficiency of solar cells, reducing the production costs, and increasing the lifetime. Energy storage is one of the important considerations for large scale use of solar energy. Solar energy is available during the day but most of the power consumption occurs in the night. So there is a need for efficient storage technology for solar energy.

Table 1. Table comparing various energy sources [24]

Energy Source	Type of Processes	Advantages	Disadvantages
Petroleum	Drilling, Oil shale	Convenient and low pollution	Limited supply, nonrenewable
Natural Gas	Drilling	Convenient and low pollution	Very limited supply, nonrenewable
Coal	Deep or strip mining, solvent refining, pyrolysis, gasification, magneto hydrodynamic usage	Easy to handle, Provides source of hydro carbons in gaseous or liquid form as well as normal solid form	Atmospheric pollution, nonrenewable

Table 1 (Continued)

Nuclear Fission	Light water reactors	Existing technology, compact	Limited fuel supply, operating and transport hazards
Solar Thermal	Direct heating and cooling via absorption of solar radiation	Pollution-free unlimited energy source	Need for extensive architectural changes, storage required
Solar electric	Use of solar energy to operate a steam turbine	Pollution-free unlimited energy source	Research needed on collection, focusing and storage
Solar Photovoltaic	Photovoltaic effect in semiconductor junction devices	Pollution-free unlimited energy source	High cost of the cells, energy storage and operating life time
Hydroelectric	Full of water gravity used to generate electricity	Renewable, inexpensive, can be used as storage process	Limited to special locations
Tidal energy	Motion of water under gravitational pull of moon used to generate electricity	Pollution-free renewable	Limited number of exploitable sites
Wind	Force of the wind used to generate electricity	Pollution-free renewable	Limited to special locations, large scale effect on weather unknown
Ocean Thermal	Uses thermal gradients to drive heat engine and generate electricity	Pollution-free renewable	Special materials problems in resisting corrosion, costly transmission
Biomass	Conversion of solid organic matter into synthetic fuel	Ready supply, could utilize wastes	Uses arable land if deliberately planted, cost uncertain, sludge disposal

1.2 Sunlight

Sun is the only long term natural resource available to us. The spectral distribution of the radiation from the sun is modified by the absorption of radiation in the solar atmosphere and the earth's atmosphere. Most of the intense radiation from the sun's deep interior is absorbed by a layer of H^- ions near the sun's surface. Sunlight is attenuated by at least 30% during its passage through the earth's atmosphere. A typical spectral distribution of sunlight reaching the earth's surface is shown in figure1. The degree of attenuation is highly variable. The most important parameter determining the total incident power under clear conditions is the length of the lightpath through the atmosphere. This is shortest when the sun is directly overhead. The ratio of any actual path length to this minimum value is known as the optical air mass (AM). When the sun is directly over head, the optical air mass is unity and the radiation is described as air mass one (AM1) radiation [27].

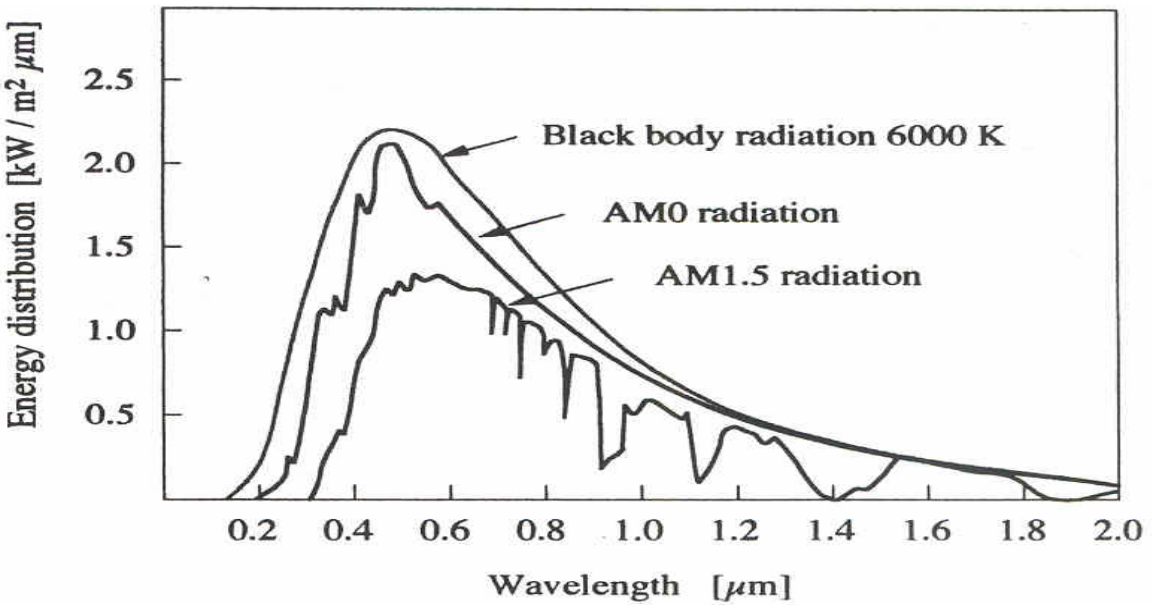

Figure 1. Spectral distribution of sunlight

1.3 Solar cells

The conventional solar cell is a pn junction with a single bandgap, E_g. Solar cells operate on the principle of the photovoltaic effect. When a solar cell is exposed to the solar spectrum, a photon with energy greater than or equal to the bandgap of the material contributes to the cell output. The wavelength of the light absorbed can be related to the energy by the following equation.

$$E = hc/\lambda \quad (1)$$

where h is Plank's constant, c is the velocity of light and λ is the wavelength of light.

The basic structure of a solar cell device is shown in figure 2. When a photon of certain energy is incident on the front surface of the device, it gets transmitted and may get absorbed in the neutral n-region, depletion region, or the neutral p-region of the device depending upon the bandgap of the material and the energy of the incident photon. This energy of the absorbed photon excites the electron from the valence band to the conduction band generating electron hole pair. The electron hole pair generated within their corresponding diffusion lengths diffuse to the depletion edge and gets drifted away by the electric field present in the depletion region to the opposite side. For this device structure, front contacts should be optically transparent and electrically conducting so that most of the light gets absorbed near the depletion region.

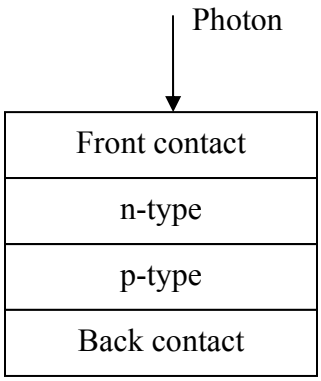

Figure 2. Basic solar cell device structure

The objective of this thesis is to explore different transparent conducting oxides which are used as front contacts in thin film solar cells. In CdTe solar cells, fluorine doped tin oxide thin films are used as highly conducting transparent conducting oxides and zinc stannate thin films are used as high resistive buffer layers. Zinc stannate films deposited at room temperature and at 400°C are studied for the high performance of CdTe solar cell.

CHAPTER 2

SOLAR CELL DEVICE PHYSICS

2.1 Semiconductor fundamentals

Consider a p-type material and n-type material. The band settings of the p-type and n-type semiconductors are shown in figure 3 where E_C is conduction band energy, E_V is valence band energy and E_F is the fermi level of a semiconductor.

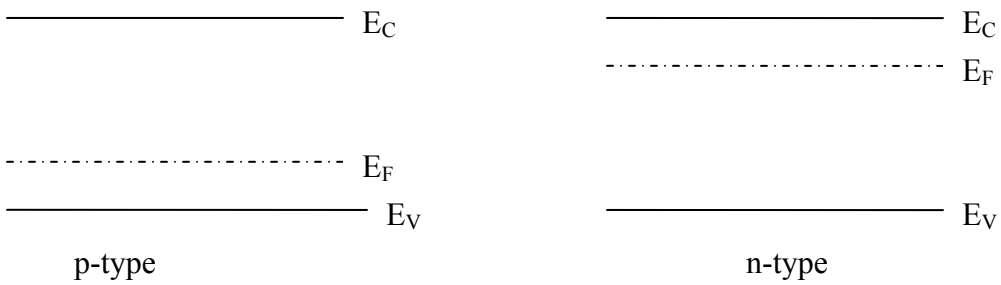

Figure 3. Fermi levels in p- type and n-type semiconductor

When a p-n junction is formed, electrons and holes move across the metallurgical junction so that the fermi level E_F becomes constant at equilibrium throughout the device. This migration, or diffusion of electrons and holes create a charge imbalance on their corresponding n side and p side by leaving behind ionized donors and acceptors. This produces a space charge region with an excess of negative charge on the p side and

excess of positive charge on the n side. This charge imbalance sets up an electric field in this region. The diffusion of carriers across the junction produces diffusion current. This diffusion continues until the strength of the electric field is sufficient enough to drift back these carriers. At this point, the junction is said to be in equilibrium. When a same material is used to form the both sides of the p-n junction but with different type of dopants, then the junction is called homojunction as shown in figure 4. The amount of band bending gives the built-in potential of the device.

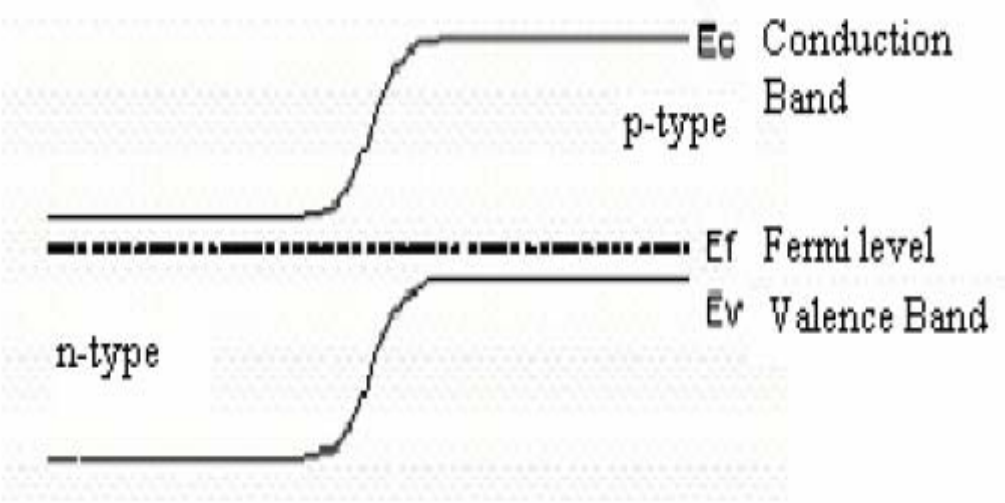

Figure 4. Band alignments in a homojunction [23]

2.1.1 Hetrojunctions

A hetrojunction is formed between two semiconductors with different band gap energies E_{g1} & E_{g2}, different work functions Φ_1 & Φ_2, different electron affinities χ_1 & χ_2. Figure 5 shows a hetrojunction where $E_{g1} > E_{g2}$

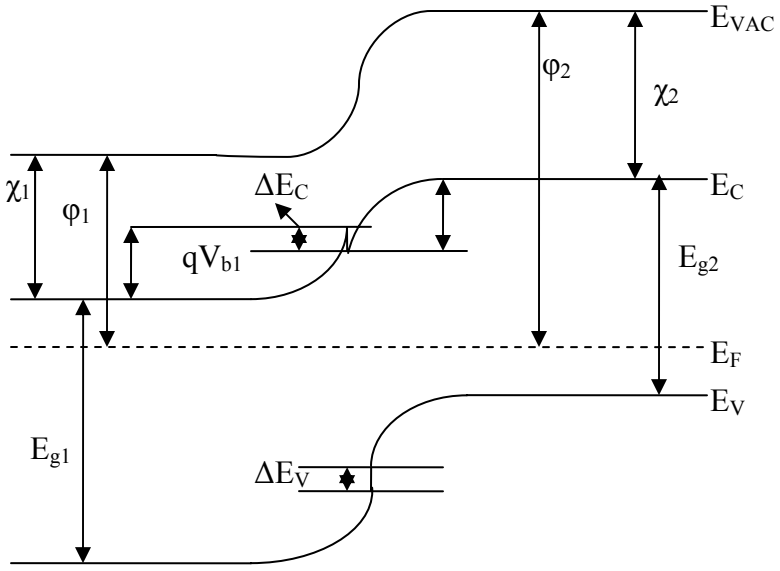

Figure 5. Band alignments in hetrojunction

ΔE_C is difference in energy of conduction bands of two semiconductors.

ΔE_V is difference in energy of valence band edges of two semiconductors

When a junction is formed between these semiconductors, there is discontinuity in the band profile due to different band gap energies and electron affinities.

$$\Delta E_C = \chi_2 - \chi_1 \quad (2)$$

$$\Delta E_V = E_{g2} - E_{g1} + \chi_2 - \chi_1 \quad (3)$$

A negative ΔE_C or ΔE_V produces a spike in the conduction band or valence band which is undesirable for photovoltaic applications. The spike impedes the flow of minority carriers across the junction from p-type to n-type regions and the photocurrent is reduced. Such spikes can be avoided by a suitable combination of material properities like electron affinities and band gap energies.

The built in potential is equal to the sum of partial built-in potentials, V_{b1} & V_{b2} or it is equal to the difference between the work functions.

$$\Delta\Phi = \Phi_2 - \Phi_1 \quad (4)$$

For hetrojunctions, the change in crystal structure across the junction is an inherent structural problem. Due to this, an interface is formed between two semiconductors. Interfaces can be efficient recombination centers because they introduce deep trap levels in the band gap. They also provide sites for quantum mechanical tunneling process which is important for current loss mechanisms across junction [28]. The origin of interface states may be due to the degree of mismatch between the crystal lattices of the semiconductor. Therefore for a good hetrojunction solar cell, a small ΔE_C and good lattice match are necessary.

2.2 Principle of operation of solar cell and solar cell physics

Figure 6 shows a p-n junction under illumination. The n-side of the junction is thin and heavily doped. By doping the n-region heavily, most of the depletion region extends into the p-region. Since the n-region is heavily doped and the lifetime of the holes, which are minority carriers on the n-side is short, use of a thin n-layer helps in avoiding recombination of holes before they reach the depletion region edge. Moreover, if the n-layer is thin, most of the light gets transmitted and absorbed in the depletion region which is very important for the collection of generated carriers. The front contact is a transparent conducting material. Light is illuminated through the front contact into the device. When the device is illuminated, as the n-side is narrow, most of the photons get absorbed in the depletion region and neutral p-region generating electron hole pairs.

The electron hole pairs generated in the depletion region drift under the influence of electric field present in the depletion region. The electrons generated by the absorption of

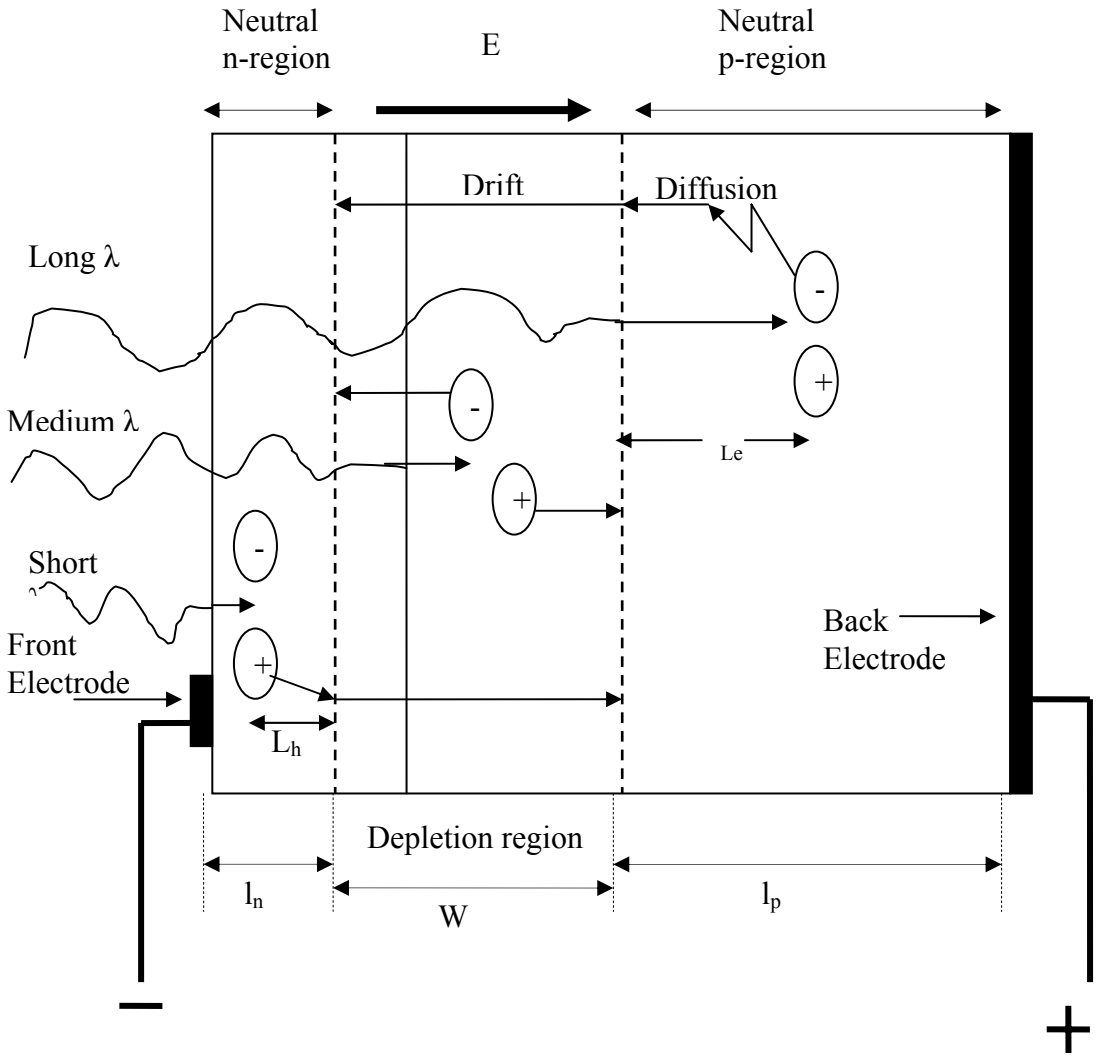

Figure 6. Principle of operation of the solar cell [25]

photons within the diffusion length of electrons in the neutral p-region diffuse to the depletion region edge and get collected. The electrons generated at a distance greater than the diffusion length from the depletion region edge are lost to recombination. Similarly the holes generated by the short wavelength photons absorbed in the n-region diffuse to

the depletion region edge and get collected. If the external terminals of the cell are shorted, current caused by this excess electron-hole transport across the junction will flow in an external circuit. The current due to the flow of photogenerated carriers is called photocurrent, and it depends on the light intensity. The current obtained under this condition is called short-circuit current (J_{SC}). Under short conditions, there is no change in the potential drop across the cell since its terminals are shorted. If the terminals of the device are open, the current in the external circuit is zero. Charge builds up on both sides of the junction due to excess electrons on n-side and excess holes on the p-side. Eventually, a field builds up in the junction whose direction is opposite to the direction of electric field in the depletion region caused by the ionized donors and acceptors. This effect reduces the height of internal barrier which allows the majority carriers in the n- and p- regions to overcome the barrier and diffuse to the opposite side of the junction. The flow of majority carriers counteracts the flow of photogenerated minority carriers. Eventually, a steady state is established in which there is no net current in the device. Now an open-circuit voltage (V_{OC}) develops between the terminals of the device with p-side positive with respect to the n-side. The J_{SC} and the V_{OC} depend on the level of incident illumination, geometry of the device and the material properties.

If an external load is connected to the solar cell, a positive voltage appears across the junction as a result of the current passing through it. This voltage reduces the built-in potential of the p-n junction [25].

The total current through the solar cell is given as:

$$I = -I_L + I_0[\exp(qV/AkT)-1] \quad (5)$$

Where I_L is photogenerated current

I_0-Reverse saturation current

A-Diode quality factor

The I-V characteristics of a typical solar cell measured both in the dark and under the illumination are shown in figure 7. Several parameters involved in the characterization of a solar cell are listed below:

I_{SC}-Short-circuit current

V_{OC}-Open-circuit voltage

I_m-Current corresponding to the maximum power point

V_m-Voltage corresponding to the maximum power point

P_{max}-Maximum power generation (Product of V_m & I_m)

FF-Fill Factor

The current I_L is the current due to illumination. P_{max} is determined from the I-V product in the 4th quadrant. Fill factor is defined as

$$FF = V_m I_m / V_{OC} I_{SC} \quad (6)$$

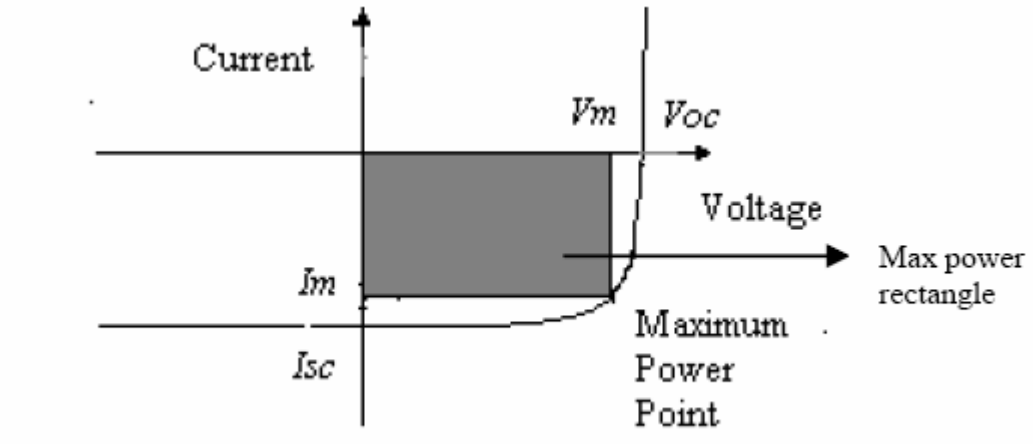

Figure 7. Typical I-V curve for an illuminated solar cell

The photovoltaic conversion efficiency (η) of the solar cell is a measure of the amount of light energy converted to electrical energy.

$$\eta = P_{max} / P_{in} \tag{7}$$

P_{in} is the incident power input to the solar cell.

Figure 8 represents the equivalent circuit of the solar cell with a series resistance R_s and a shunt resistance R_{sh}. The current–voltage relationship equation with series and shunt resistance effects included is given by

$$I = I_0[\left(\exp q\,(V\text{-}IR_s)\,/AkT\right)\text{-}1] + (V\text{-}IR_s)/R_{sh} - I_L \tag{8}$$

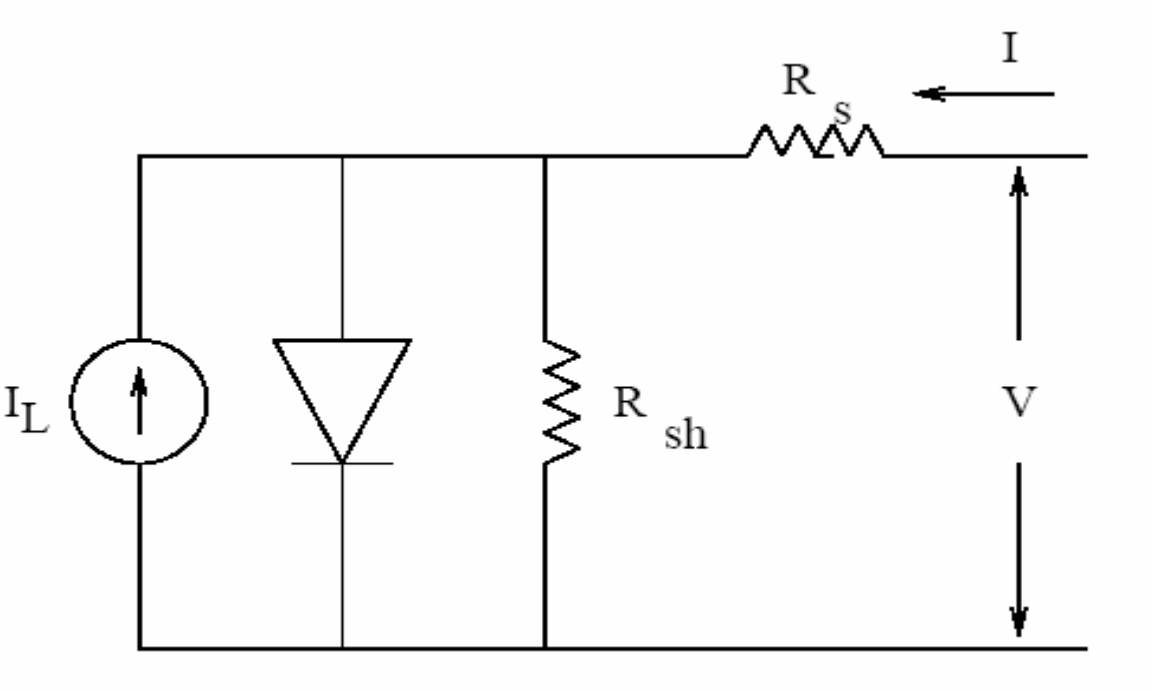

Figure 8. Equivalent circuit of a solar cell with series and shunt resistances, R_s & R_{sh} [26]

Generally, the R_s can be approximated from the slope of a J–V curve at higher current values in the first quadrant and R_{sh} can be approximated from the slope of a J-V curve in

the third quadrant where J is the current density of the device. For an ideal solar cell, the R_s is zero and R_{sh} is infinity. But, in practice, due to various reasons, the series resistance has some finite value greater than zero and shunt resistance is reduced. Lower shunt resistances are mainly due to the formation of defects like pinholes. Fill factor and V_{OC} are greatly affected by low R_{sh}. Low R_{sh} also induce leakage currents which affect the J_{SC} of the device. Series resistance is mainly caused due to the resistances at the contacts and in the bulk of the device material. Fill factor and short circuit current are affected by higher series resistances. [26]

CHAPTER 3

TRANSPARENT CONDUCTING OXIDES AND LITERATURE REVIEW

3.1 Transparent conducting oxides

Transparent conducting oxides (TCOs), as the name implies are transparent as well as conductive. High transparency combined with useful electrical conductivity is achieved by selecting a wide bandgap oxide that is rendered degenerate through the introduction of native or substitutional dopants. Transparent conducting oxides, because of their high transmission and required conductivity, have diverse applications. The ability of TCOs to reflect thermal infrared heat is used to make energy conserving windows also known as low emissive windows. The electrical conductivity of TCOs is exploited in front surface electrodes for solar cells and flat-panel displays where high transmission of the front electrodes is also important. In aircraft and automobile windows, TCOs offer advantages of thermal management and also act as thin film resistive heater elements for demisting and deicing windows. Transparent conducting oxides are also used in electrochromic windows. Electrical induced reduction results in an electrically controllable change in color and light transmission. This effect can be used in the design of smart windows. Transparent conducting oxides can be formed into transparent electro magnetic shields, invisible security circuits on windows, and transparent radio antennas built into automobile windows. [2]

3.1.1 Optical properties

The optical properties of a TCO depend on its material properties such as bandgap and the plasma edge frequency. They also depend on the thickness of the material. When light is incident on the surface of a TCO, it may be absorbed, transmitted and reflected depending upon the above mentioned material properties. If the energy hν of the incident photon is greater than or equal to the band gap of the material, then that photon is absorbed. This absorbed photon energy aids in the electron transition from valence band to the conduction band. The amount of light absorbed in a thin film semiconductor depends on the material's wavelength dependent absorption coefficient as shown in equation 9.

$$\alpha(\lambda) = C\,(h\nu - E_g^{d})^{1/2} \tag{9}$$

where α is the absorption coefficient, h is the Plank's constant, ν is the frequency, E_g^{d} is the direct bandgap of the material and C is a constant. The plot of α^2 against the photon energy (hν) yields a straight line whose intercept with the energy axis gives the bandgap of the material. The amount of light absorbed can be related to the thickness of the material by the following expression

$$\alpha = \left(1/t\right) \ln\left(1/\left(1-A\right)\right) \tag{10}$$

where t is the thickness and A is the absorptance at specific wavelength. [22]

If the energy of the incident photon is less than the bandgap, then the photons are transmitted. The important optical characteristic of TCOs is that they have a transmission window between wavelengths of about 0.4 μm and 1.5 μm. At longer wavelengths, reflection occurs due to the plasma edge. After the absorption edge from the bandgap, a major portion of the light that is not transmitted is reflected. This reflection is because of

both the surface and bulk of the material. Reflection is greater in the near infrared region of the spectrum. This reflection is dominated by bulk reflection that occurs as a result of photon–electron interactions, which induce scattering mechanisms. Electrons and photons interact due to the electromagnetic nature of the photon. The frequency at which this reflection takes place is called plasma frequency given by the following expression

$$\omega_p = (ne^2/\varepsilon_0\varepsilon_\infty m_c^*)^{1/2} \quad (10)$$

where n is the carrier concentration, e is the electronic charge, ε_0 is the permittivity of the free space, ε_∞ is the high frequency permittivity and m_c^* is the conductivity effective mass [5].

Spectral dependence of a semiconducting transparent material is shown in figure 9. At frequencies higher than the plasma frequency, electrons cannot respond and the material behaves as a transparent dielectric. At frequencies below the plasma frequency, TCO reflects and absorbs incident radiation. For most of the TCOs, the plasma frequency falls in the near-infrared part of the spectrum and the visible region is in the higher and transparent frequency range [1].

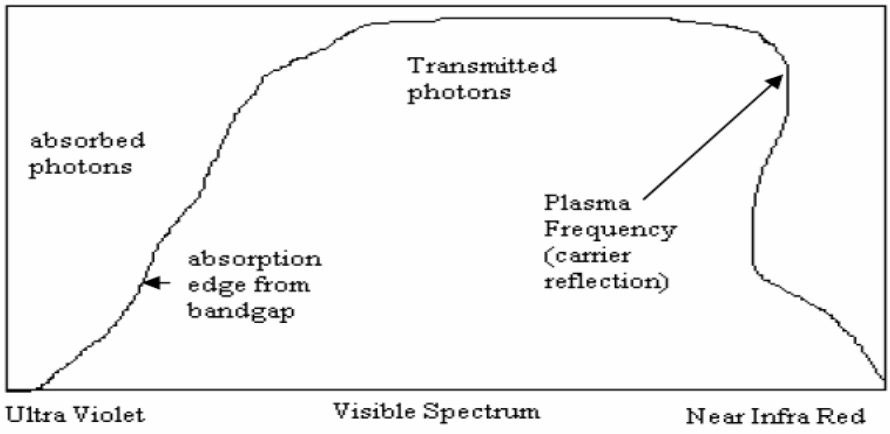

Figure 9. Spectral dependence of a semiconducting transparent material

3.1.2 Electrical properties

Electrical conductivity mainly depends on the carrier concentration and mobility of the free carriers. Electrical conductivity is given by the following expression

$$\sigma = qn\mu \tag{11}$$

where n is the carrier concentration and μ is the carrier mobility. Conductivity can be increased either by increasing the carrier concentration or mobility. The increase in the free carrier concentration also increases the free carrier absorption which effects the transmission of the TCO. On the other hand, mobility can be expressed as

$$\mu = q\tau / m_c^* \tag{12}$$

where τ is relaxation time and m_c^* is the conductivity effective mass. Electron mobility is also determined by the electron scattering mechanisms that operate in the material. At low doping levels, scattering of electrons by phonons is present. However in practical applications, TCOs with high doping levels are used. Under these conditions, scattering by ionized dopant atoms becomes the important scattering phenomenon. In polycrystalline films, grain boundary scattering is present. All these scattering mechanisms limit the mobility. One way of increasing the mobility is by increasing the relaxation time. This can be done by producing high quality films with fewer defects and improved orientation. Another way of increasing the mobility is by decreasing the effective mass [5].

As the increase in carrier concentration increases the free carrier absorption, increasing the mobility is the most effective way of increasing conductivity without affecting the material's optical properties.

3.1.3 Compromise between optical and electrical properties

Figure 10 shows the variation of the modeled reflectance of a film with wavelength for different carrier concentrations. Free carrier mobility is assumed to be constant in this case with carrier concentration, although this may not be achieved in practice.

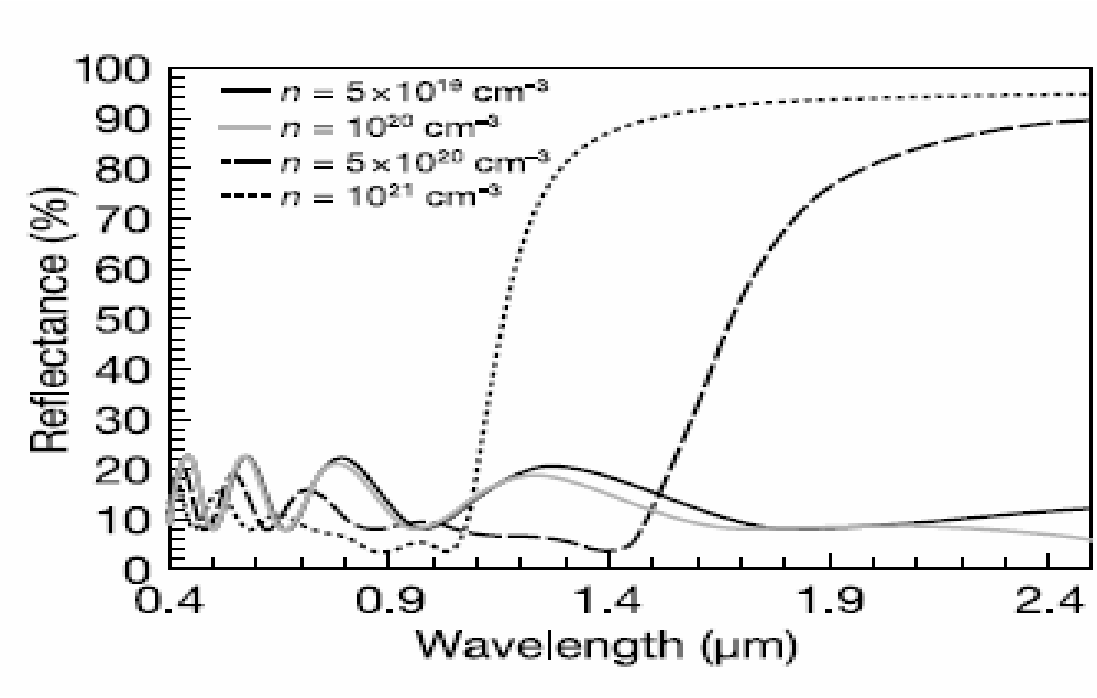

Figure 10. Spectral dependence of reflectance of TCOs with different carrier concentrations [5]

The carrier concentration is varied between 5 X 10^{19} cm^{-3} and 1 X 10^{21} cm^{-3}. Assumed high frequency permittivity and electron effective mass are 4 and $0.3m_e$ respectively. Film thickness is 0.5μm. For the two higher carrier concentrations, the plasma wavelength changed from approximately 1.6 μm to about 1.1 μm following the relation mentioned in equation 10. A mean reflectance of about 15% is observed in the visible range of wavelengths due to interference fringes. Beyond the plasma wavelength, reflectance is about 90%. Films with low carrier concentration did not exhibit plasma frequency reflectance.

Figure 11 shows the variation of absorptance with wavelength for the same parameters used in figure 10. As the carrier concentration is increased, the height of free carrier absorption band increased because there are more carriers available to absorb photons.

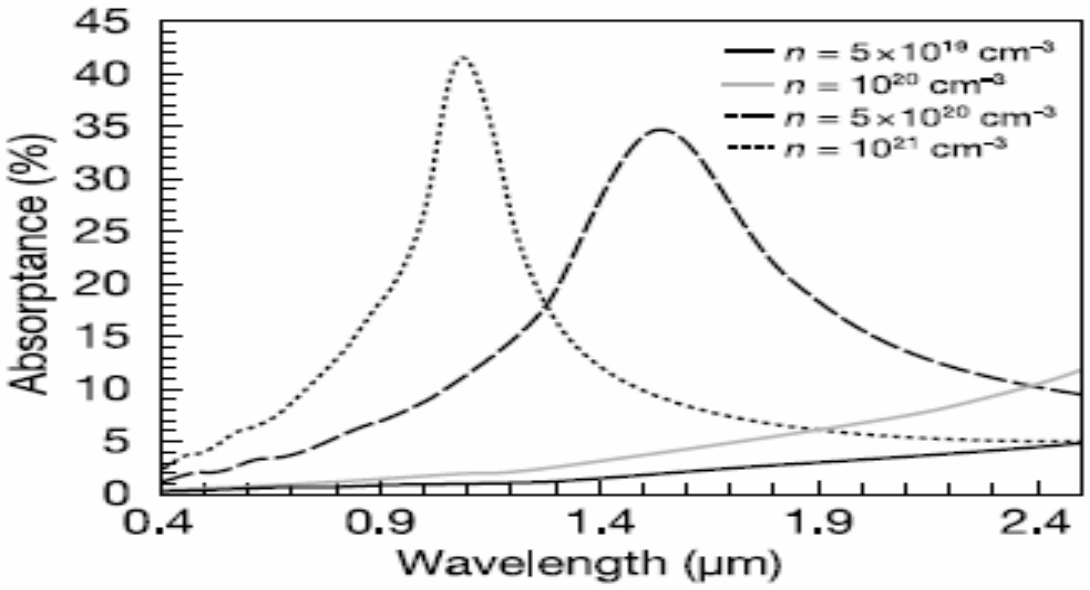

Figure 11. Spectral dependence of absorptance of TCOs with different carrier concentrations [5]

Figure 12 shows the modeled variation of absorptance with wavelength for a film with different mobilities. The carrier concentration is kept constant at 5 X 10^{20} cm^{-3}. As the mobility is increased, the wavelength at which the peak of absorption occurred did not change but the height of the free carrier absorption band decreased. Thus by increasing the mobility, the conductivity of TCO can be increased without compromising its optical properties [5].

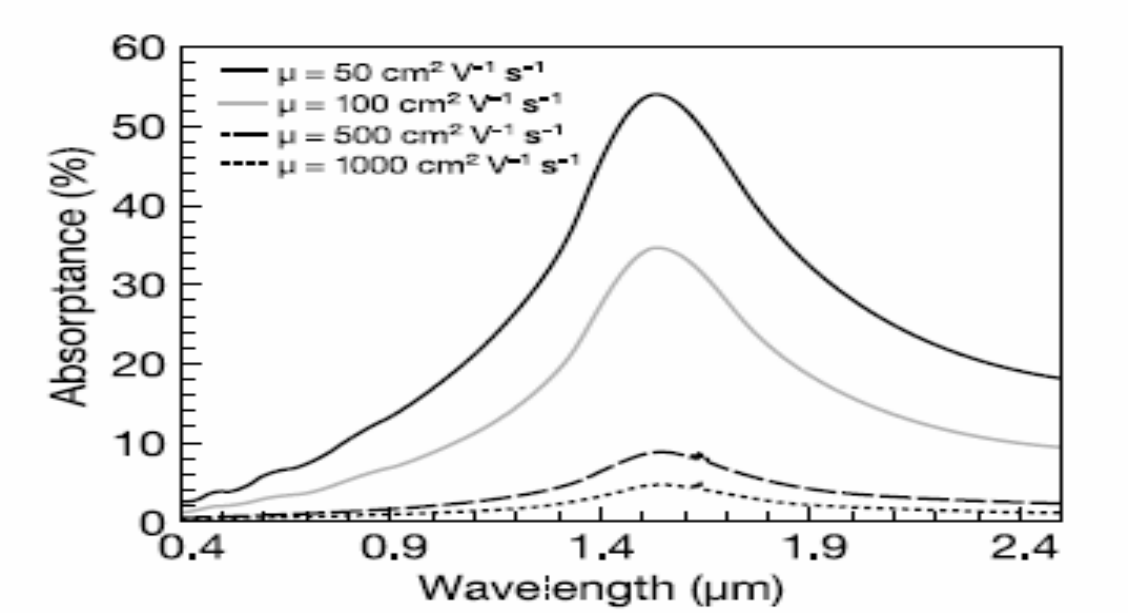

Figure 12. Spectral dependence of absorptance of TCOs with different mobilities [5]

An effective TCO should have high electrical conductivity combined with low absorption of visible light. A figure of merit for TCOs can be expressed as follows

$$\sigma / \alpha = - \left\{ R_S \ln \left(T+R \right) \right\}^{-1} \tag{13}$$

where R_S is the sheet resistance in Ω/□, T is the total visible transmission and R is the total visible reflectance. A larger value of σ/α indicates better performance of the TCO [4].

3.2 Transparent conducting oxide materials

Most of the research to develop highly transparent and conductive thin films is focused on n-type semiconductors consisting of metal oxides. These TCOs may be classified as binary compound or multicomponent oxide materials. Binary compound TCO materials which are in practical use, include SnO_2: F or SnO_2: Sb, In_2O_3: Sn (indium tin oxide

films) and ZnO: Al or ZnO: Ga. Multicomponent oxides which are in practical use include Cd_2SnO_4, $CdIn_2O_4$, Zn_2SnO_4 and $GaInO_3$. Transparent conducting oxides used in this work are SnO_2: F, Cd_2SnO_4, undoped SnO_2 and Zn_2SnO_4.

3.2.1 SnO_2: F

Doped tin oxide is a n-type wide band gap degenerate semiconductor. The properties of SnO_2 depend on the deviation from stoichiometry such as oxygen deficiencies and on the dopants used. Tin oxide crystallizes in the rutile structure. The Sn atoms are on a body centered tetragonal lattice and oxygen atoms in a hexagonal closed packed structure. The rutile structure is shown in figure 13. Each Sn cation has a coordination number of six, forming an octahedral geometry with anionic oxygen present. If SnO_2 is perfectly stoichiometric, it would be an insulator or at most an ionic conductor. However, in practice, the material is never stoichiometric. It is anion deficient due to the formation of oxygen vacancies in the perfect crystal. These vacancies are responsible for making electrons available for the conduction process. Ionized oxygen vacancies predominate in SnO_2 according to the following defect reaction.

$$Sn^x_{Sn} + 2O^x_O \leftrightarrow Sn^x_{Sn} + 2V^{\bullet\bullet}_O + 4e + O_{2\,(g)} \qquad (14)$$

where Sn^x_{Sn} and O^x_O represent bonded tin and bonded oxygen respectively; $V^{\bullet\bullet}_O$ represents oxygen vacancy [1]. Even a perfectly stoichiometric SnO_2 crystal can be made conducting by creating oxygen deficiencies by heating the film in a slightly reducing atmosphere. The other method of making SnO_2 conducting is by chemical doping, for example, by fluorine or antimony. Either the doping of cation or anion sites by higher valency impurities in the oxide materials increases the n–type conductivity.

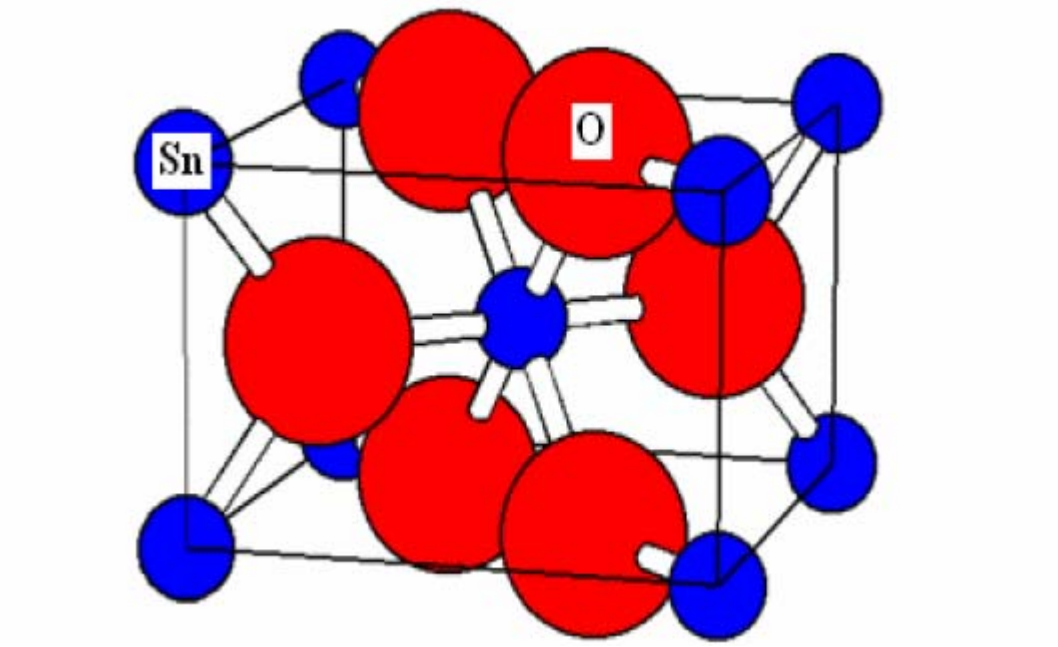

Figure 13. Structure of tin oxide [23]

Fluorine doped tin oxide film with a thickness of 5000Å has an average transmission of 83.3% as shown in figure14 [22]. The loss in transmission is mainly due to reflection. The average reflection in the visible region is 13.2% and the average absorption is 3.6%. SnO_2: F films are deposited by chemical vapor deposition using TMT (Tetra Methyl Tin) and oxygen at 450°C. SnO_2: F films are polycrystalline in the as- deposited form. XRD spectra from figure 15 shows that the preferred orientation is along [110] direction.

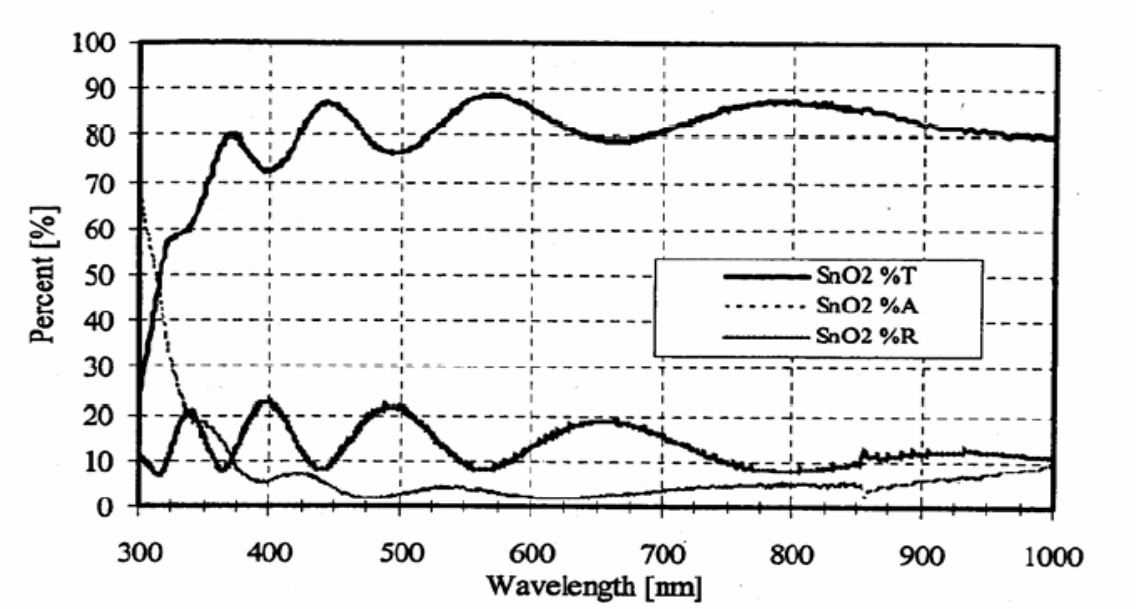

Figure 14. Optical transmittance, reflectance and absorptance of SnO_2: F film [22]

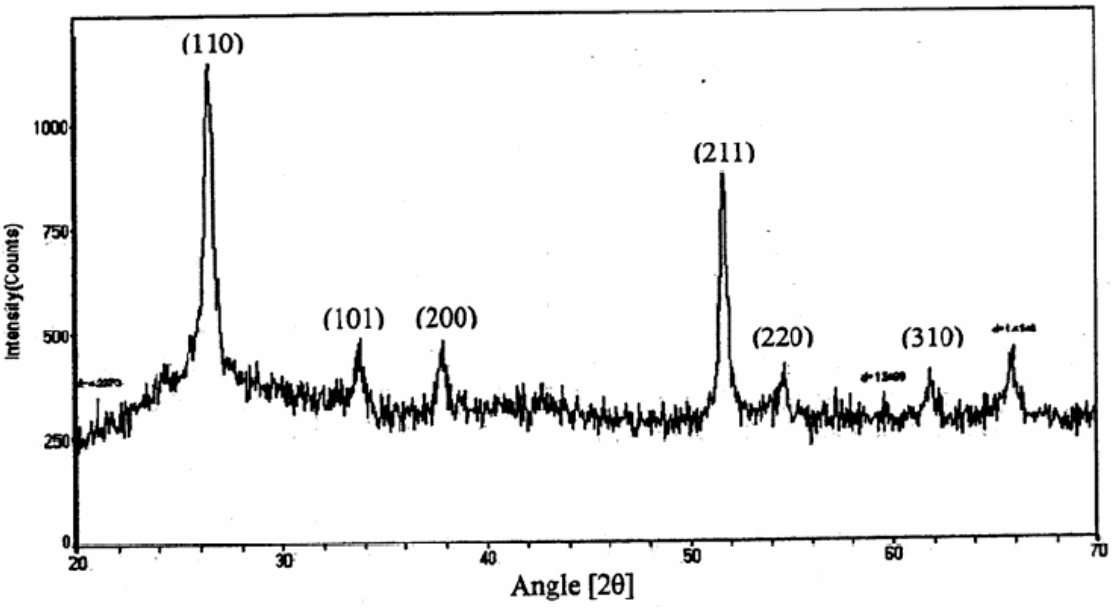

Figure 15. X-ray diffraction pattern for CVD deposited SnO_2: F [22]

3.2.2 Cd_2SnO_4

Cd_2SnO_4 is a ternary mixed metal oxide. The lowest energy crystal structure is the thermodynamically stable orthorhombic system. However, sputtered films are of high quality and crystallize in both the spinel and inverse spinel structures [10]. Half of the cadmium cations occupy tetrahedral sites and the remaining half are distributed with tin cations on the octahedral sites ($Cd[SnCd]O_4$). Oxygen ions are in face centered cubic close packing. The conductivity in Cd_2SnO_4 is mainly due to defects in its structure. The possible defects in Cd_2SnO_4 are $Sn_{Cd,}$ Cd_I, V_{Cd}, Cd_{Sn} and V_O which represent Sn on Cd antisite, Cd interstials, Cd vacancies, Cd on Sn antisite and Oxygen vacancies respectively. Among these defects, Sn_{Cd} and Cd_I are shallow donors; V_O is a deep donor; V_{Cd} is a shallow acceptor and Cd_{Sn} is a deep acceptor. Of all these defects, the formation of Sn_{Cd} antisites is energetically favorable which is responsible for the n-type conductivity of unintentionally doped Cd_2SnO_4. Cd_2SnO_4 can be made conductive through the creation of a Cd-rich growth environment. The Cd–rich growth environment is to generate a Sn–rich environment in the lattice as a result of the chemical potentials, μ_{Sn} and μ_{Cd} being co-dependant. The high conductivity of Cd_2SnO_4 can be attributed to the high mobility of carriers. This is probably because of the high degree of structural order of Cd_2SnO_4 films due to which longer relaxation times are obtained. Mobilities as high as 80 $cm^2V^{-1}s^{-1}$ have been obtained. [9, 10, 11]. Figure 16 shows the optical transmission for Cd_2SnO_4 films with a thickness of 2000Å and annealed in He and H_2. Hydrogen, a reducing agent, increased the material's carrier concentration.

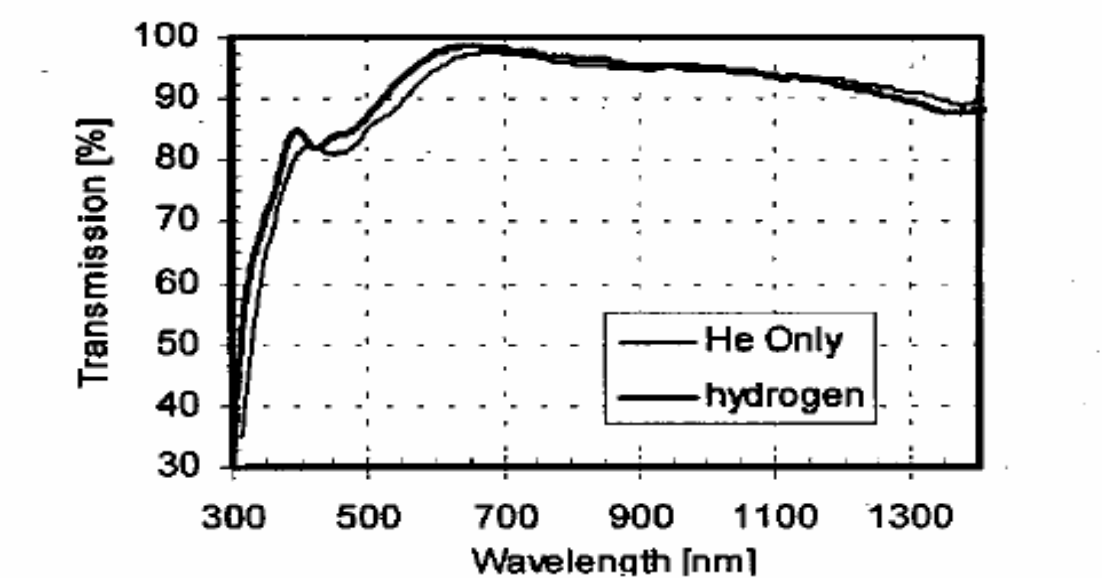

Figure 16. Optical transmission of Cd_2SnO_4 films with a thickness of 2000Å before and after H_2 annealing [18]

In the short wavelength range of 300-400 nm, a slight shift in the absorption edge exists as a result of H_2 annealing. This might be a Moss-Burstein shift due to the increased electron density. The slight increase in reflection in the infrared region might be a free carrier reflection due to the increased carrier concentration [18].

Cd_2SnO_4 films have better optical properties compared to conventional TCOs. This is due to the lower resistivities of Cd_2SnO_4 films, which allow thinner films to be used. Figure 17 compares the transmission and absorption of Cd_2SnO_4 and SnO_2 films with similar sheet resistivities. The absorbance of the Cd_2SnO_4 film in the visible range is much lesser than that of SnO_2 film [15].

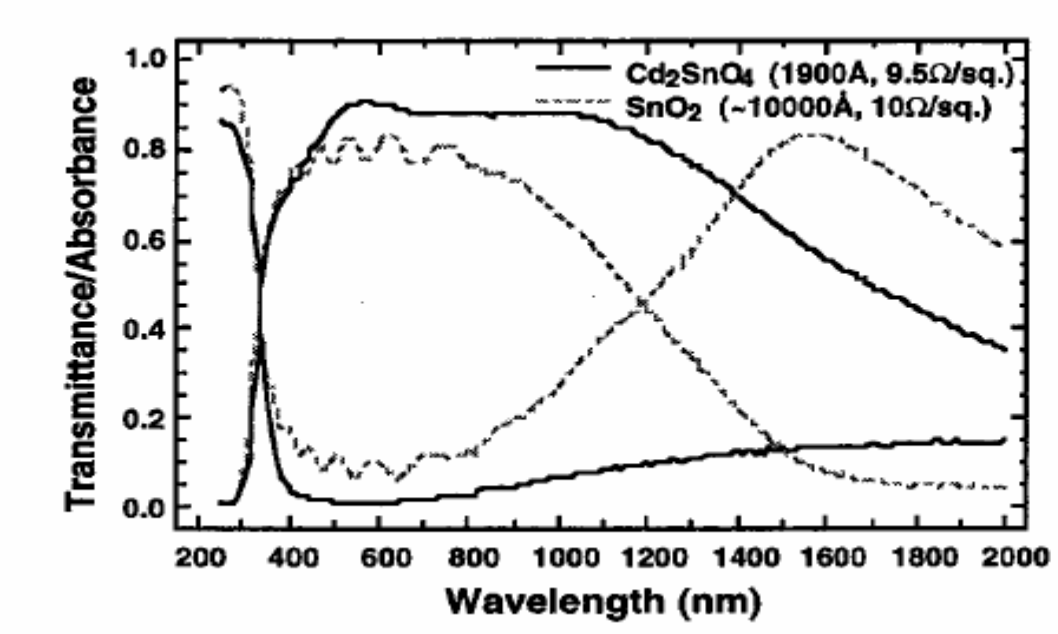

Figure 17. Transmission and absorbance of a Cd_2SnO_4 and SnO_2 film with a sheet resistivity of ~10Ω/□ [15]

3.2.3 Zn_2SnO_4

3.2.3.1 Structural properties

Zn_2SnO_4 is an inexpensive, optically transparent and electrically conducting oxide. Zn_2SnO_4 has superior optical transparency but lower electrical conductivity by several orders of magnitude than Cd_2SnO_4 films. Zinc stannate has two different oxides with different crystallographic structures and zinc to tin ratios: $ZnSnO_3$ and Zn_2SnO_4. $ZnSnO_3$ crystallizes in the orthorhombic phase and Zn_2SnO_4 crystallizes in the inverse spinel structure with half of the Zn cations occupying the tetrahedral sites and the remaining half are distributed with tin cations in the octahedral site. This spinel lattice is locally distorted enough to form two distinct octahedrally coordinated Sn and Zn sites. The two Sn and Zn octahedral sites in the lattice significantly limit the mobility of the carriers, possibly by disrupting the edge-sharing nature of the octahedral sites and thereby forming the open circuits in the conductive path ways [13].

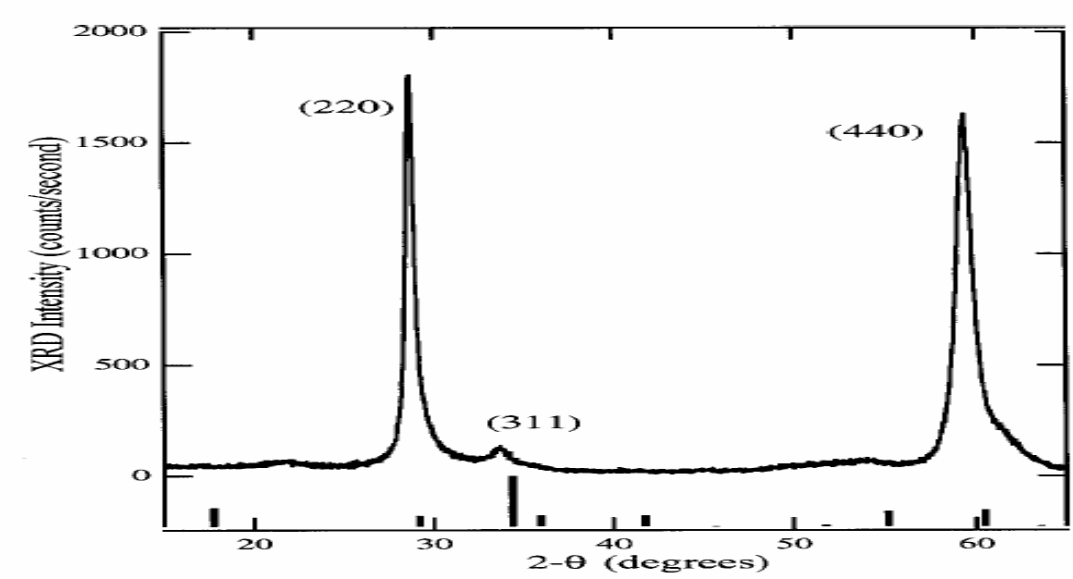

Figure 18. XRD pattern for a Zn_2SnO_4 film grown at 550°C [14]

Figure 18 shows the XRD pattern of a film deposited by RF sputtering in Ar at substrate temperatures of 550°C. It shows a preferred orientation of (220). As-grown films at room temperature are amorphous in nature. Subsequent annealing at higher temperatures makes these films polycrystalline. Figure 19 shows an AFM image of a sample grown at 600°C in Ar. The image reveals grains of 100nm in diameter and a surface roughness of 4.3nm. This unusually smooth surface is one of the qualities that is thought to make Zn_2SnO_4 ideal as a buffer layer in solar cells [14].

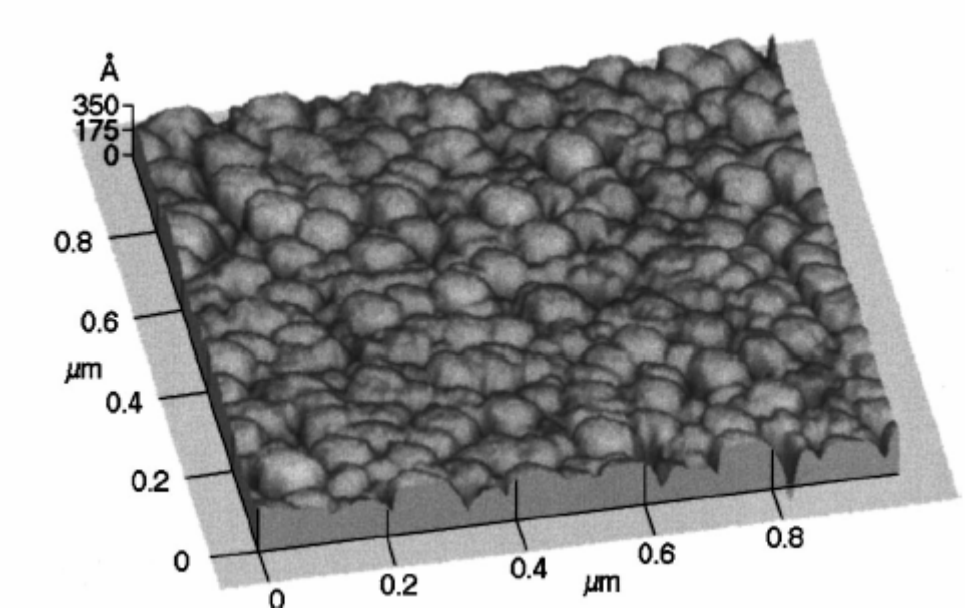

Figure 19. AFM image of a Zn_2SnO_4 film grown at 600°C in Argon [14]

3.2.3.2 Optical properties

Figure 20 shows the transmittance, reflectance, and absorptance of a Zn_2SnO_4 film for wavelengths between 300 and 2500nm.

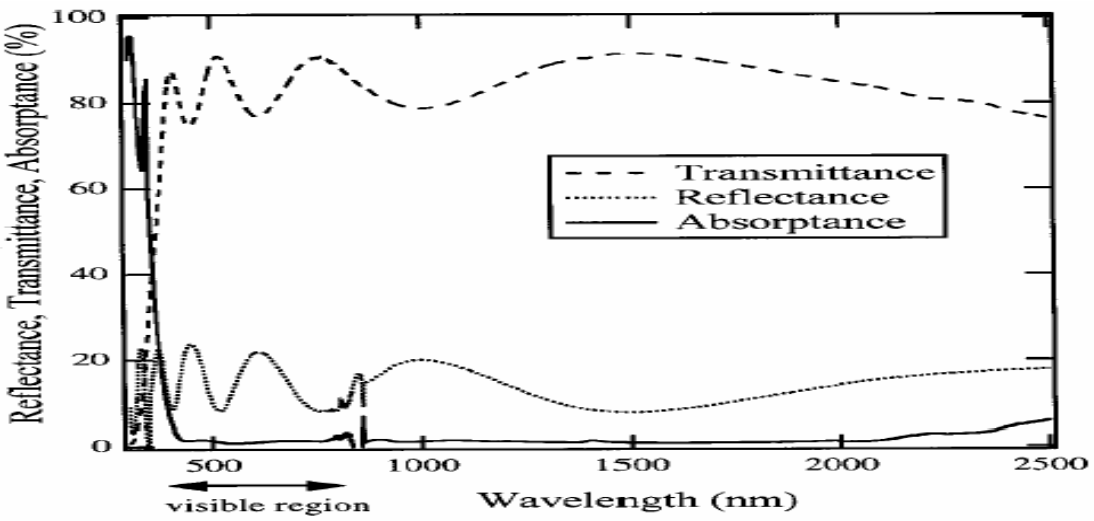

Figure 20. Percent transmittance, reflectance and absorptance vs wavelength for a Zn_2SnO_4 film [14]

Optical data on Zn_2SnO_4 films reveal that the material is highly transparent due to its low absorptance in the visible region which is less than 1.5%. The slight rise in the absorption curve near 2300 nm is due to the onset of absorption by free electrons in the conduction band. The sharp increase in the absorptance near 350nm is due to the direct band gap of the material. The direct bandgap absorption-edge wavelength highly depends on the carrier concentration in the films. Figure 21 shows the shift in the absorption edge wavelength with varying carrier concentration indicating a Moss-Burstein shift. The band gap shifted from 3.35eV to 3.89eV with increasing carrier concentration [14]

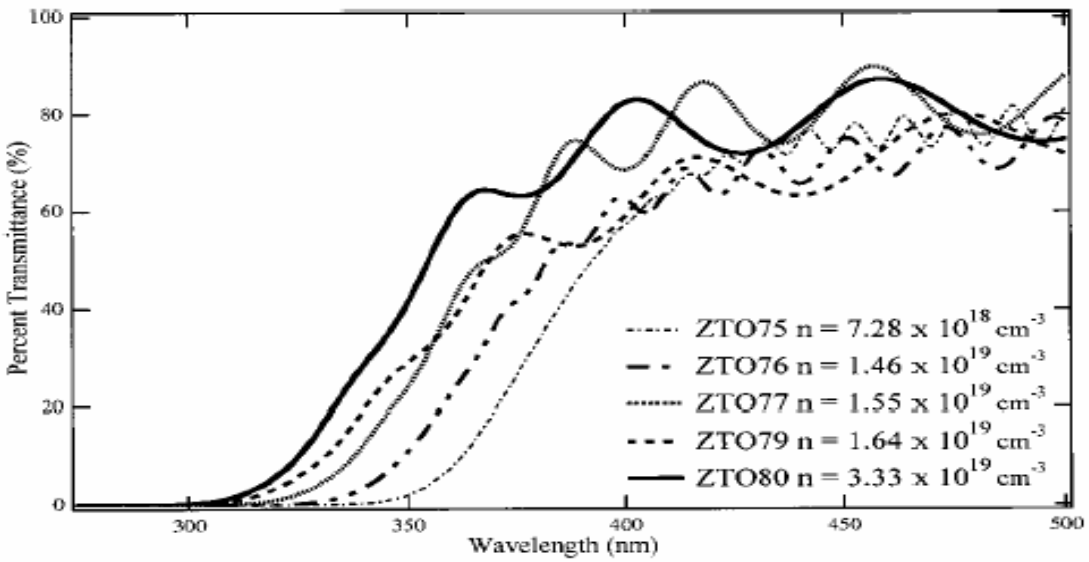

Figure 21. Percent transmission vs wavelength for Zn_2SnO_4 film with different carrier concentrations [14].

3.2.3.3 Electrical properties

Zn_2SnO_4 films are resistive compared to other conventional TCOs. Low mobilities (< 27 $cm^2/V\text{-}s$) and carrier concentrations (< $4X10^{19}cm^{-3}$) account for the low resistivities. The increase in carrier concentration in the films annealed in reducing atmosphere and decrease in carrier concentration in the films annealed in oxidizing atmosphere indicate that oxygen vacancies might be the possible mechanism for the generation of carriers.

Low mobilities in Zn_2SnO_4 films can be attributed to the short relaxation times. High density of defects responsible for the poor quality of the film limits the relaxation time of the carriers. Relatively low effective mass values in Zn_2SnO_4 films compared to other TCO materials is the reason for the large Burstein-Moss shift observed in the optical properties of the film [17].

3.3 Zn_2SnO_4 as a buffer layer in CdS/CdTe solar cells

There is a significant photocurrent loss in CdS/CdTe solar cells due to window-layer CdS bandgap absorption below 520nm. With decrease in CdS thickness, there is an increase in the device short-circuit current (J_{SC}). However, the open-circuit voltage (V_{OC}) and fill factor (FF) tend to decrease as the CdS is thinned [19]. In order to increase the device J_{SC} without affecting V_{OC} and fill factors, there is a need for consumption of CdS in the device during the processing itself. By integrating the Zn_2SnO_4 film into a CdS/CdTe solar cell as a buffer layer, interdiffusion consumes the CdS film from both the Zn_2SnO_4 and CdTe sides during the device fabrication process and improves the quantum efficiency at shorter wavelengths. The Zn_2SnO_4 film acts as a Zn source to alloy with the CdS film, which results in the increase in the bandgap of the window layer and in the short circuit current density. This interdiffussion can also significantly improve the device adhesion after $CdCl_2$ treatment, thus providing much greater latitude when optimizing $CdCl_2$ process step. The optimum $CdCl_2$ treated CdTe device has high quantum efficiency at longer wavelengths because of its good junction properties and well passivated CdTe film [20].

On the other hand, Cd_2SnO_4, because of its superior electrical and optical properties, can serve as a better replacement for conventional TCOs like SnO_2. CdS/CdTe solar cells with Cd_2SnO_4 as TCO yield improved short-circuit densities (J_{SC}). Figure 22 shows the relation between J_{SC} and transmission of Cd_2SnO_4 and SnO_2 films [16]. Replacing the 10000Å SnO_2 film with a Cd_2SnO_4 film in CdTe solar cell yielded an increase in J_{SC} of more than 1.5 mA/cm^2 [15].

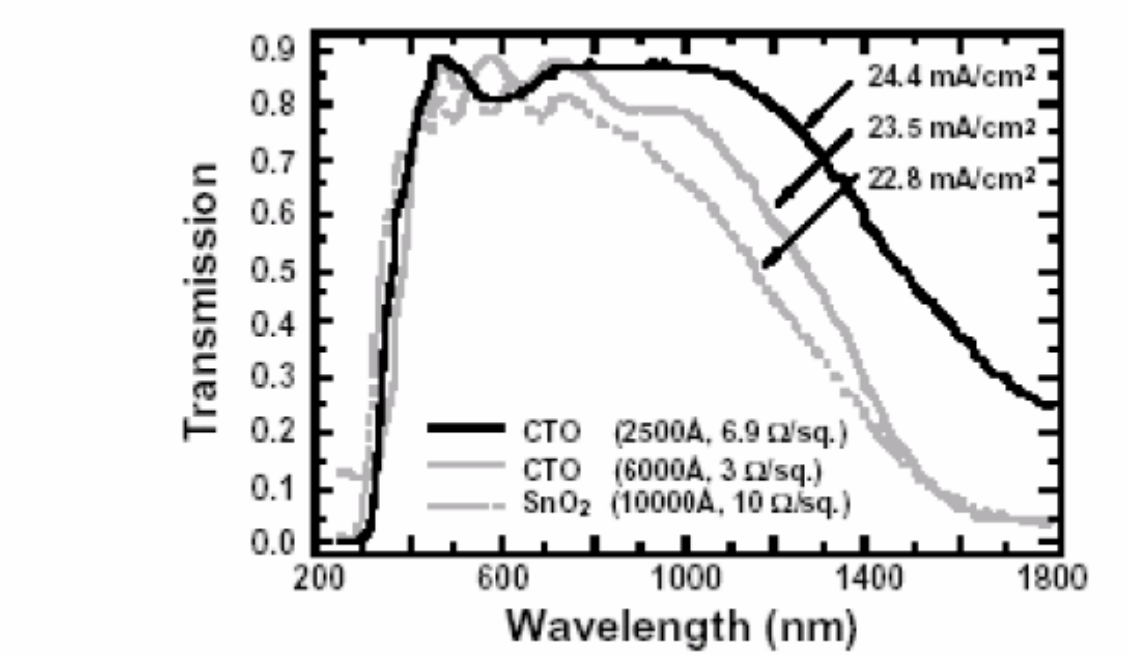

Figure 22. Relation between J_{SC} and transmission of Cd_2SnO_4 and SnO_2 films [15]

Table 2 shows the J_{SC} loss due to glass/TCO absorption for three CdTe cells on different TCO superstrates. It can be seen that the Cd_2SnO_4 based cell has the lowest J_{SC} loss (0.7 mA/cm^2) which is two to four times lower than SnO_2 based cells prepared by TMT and $SnCl_4$ precursors respectively. Figure 23 shows the modified device structure of CdTe solar cell with the inclusion of Cd_2SnO_4 and Zn_2SnO_4.

Table 2. J_{SC} losses in different TCOs [16]

TCO	R_S (Ω/Sq)	Glass/TCO Absorption loss(mA/cm^2)
$SnO_2(SnCl_4)$	8-10	2.8
SnO_2(TMT)	6-8	1.3
Cd_2SnO_4	6-8	0.7

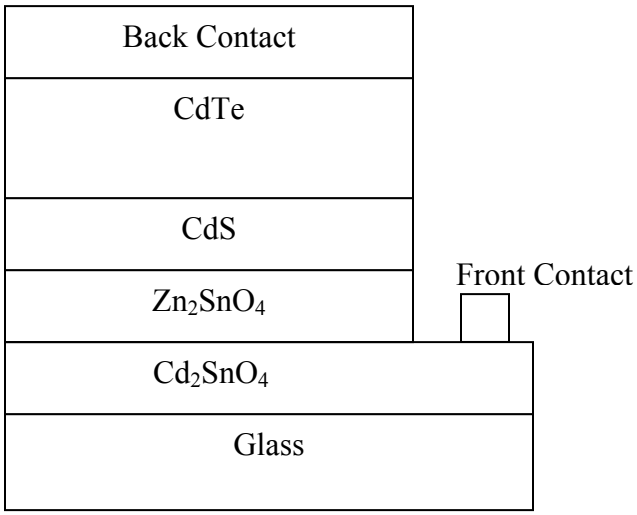

Figure 23. Modified CdS/CdTe device structure [16]

Table 3 consists of I-V data of the CdS/CdTe solar cells with different device structures. The use of a Zn_2SnO_4 buffer layer for both SnO_2 and Cd_2SnO_4 based solar cells showed improvement in all the device parameters of the solar cell thereby increasing the efficiency of the solar cell. Cd_2SnO_4 based solar cells show their

dominance over SnO_2 based solar cells because of its superior electrical and optical properties as discussed earlier in this chapter. Table 4 summarizes the parameters of the highest efficiency CdS/CdTe solar cell achieved by NREL [23].

Table 3. I-V data of CdTe solar cells with different device structures [20]

Device Structure	V_{OC}(mV)	J_{SC} (mA/cm^2)	FF(%)	η(%)
SnO_2 /CdS/CdTe	806.7	22.61	74.02	13.5
Cd_2SnO_4/CdS/CdTe	805.2	23.53	73.77	14.0
SnO_2 /Zn_2SnO_4/CdS/CdTe	830.1	24.10	74.15	14.8
Cd_2SnO_4/Zn_2SnO_4/CdS/CdTe	844.3	25.00	74.82	15.8

Table 4. The parameters of the highest efficiency CdS/CdTe solar cell achieved by NREL [23]

Cell #	V_{OC}(mV)	J_{SC} (mA/cm^2)	FF(%)	η(%)	Area(cm^2)
W547-A	847.5	25.86	74.45	16.4	1.131
W567-A	845.0	25.88	75.51	16.5	1.032

CHAPTER 4

EXPERIMENTAL METHODS

This chapter discusses various processing and characterization techniques used for the fabrication and characterization of thin films and solar cells.

4.1 Processing

4.1.1 Substrate cleaning

Corning 7059 borosilicate glass with dimensions 1.25" X 1.45" X 0.032" is used as a substrate. The substrates are cleaned in a 10% by volume HF solution; after a brief dip (7-10 secs), the substrates are rinsed thoroughly in deionized water and then dried.

4.1.2 Chemical vapor deposition of SnO_2:F

Tin oxide is deposited by the chemical vapor deposition (CVD) technique. The CVD chamber used for the deposition of SnO_2 is shown in figure 24. It consists of a quartz tube within which a substrate holder heated by RF coils is placed. The deposition is done at 450°C. The precursors used are Tetra Methyl Tin (TMT) (Sn source) and O_2. Tin oxide films are doped with Fluorine by introducing $CFBr_3$, a commercially available Freon. All the gases are introduced into the chamber using Mass Flow Controllers (MFC). The oxidation chemical reaction for this process is as follows:

$$Sn(CH_3)_{4\,(Vap)} + 8O_{2\,(gas)} \rightarrow SnO_{2\,(solid)} + 4CO_{2\,(gas)} + 6H_2O_{\,(gas)} \quad (15)$$

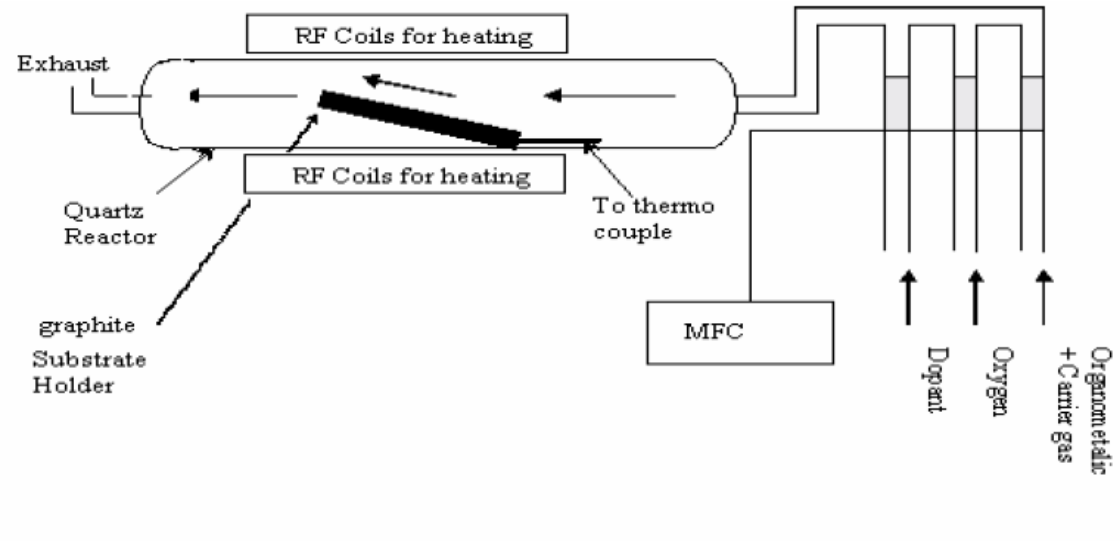

Figure 24. Schematic diagram of the CVD reactor used for SnO_2:F deposition [23]

4.1.3 Sputtering of Zn-Sn-O (ZTO)

ZTO films are prepared by RF magnetron co-sputtering of SnO_2 (99.999% purity) and ZnO (99.999% purity) targets. ZTO films are deposited at room temperature and at 450°C in Ar ambient. Cadmium stannate (Cd_2SnO_4) films are prepared by RF magnetron co-sputtering of SnO_2 (99.999% purity) and CdO (99.999% purity) targets at room temperature in Ar ambient. By co-sputtering, one can control the individual composition of each material in the compound film controlling the deposition rates of the constituent oxides.

A schematic of the sputtering chamber is shown in figure 25.The vacuum chamber used is a Consolidated Vacuum Corp. model, magnetron sputtering sources are Kurt J. Lesker Torus TRS3FSA models and power supplies are Advanced Energy RFX-600 models. The sputtering sources are positioned such that the center line of each gun created an angle of approximately forty degrees with respect to a plane parallel to the

substrate holder. To ensure uniformity in film thickness, the substrate holder is rotated during the deposition. Before each deposition, the chamber is pumped down to a base pressure of 4 X 10^{-5} torr. The operating pressure for ZTO and cadmium stannate films is 2 X 10^{-3} torr and 3 X 10^{-3} torr respectively.

After the sputter deposition, in order to improve the crystallinity, films are subjected to high temperature annealing. This is carried out in an evacuated closed end quartz tube with a vacuum line outlet and a gas inlet. Two graphite substrate holders, one on which the substrates are placed and the other on top of the substrates are used. High temperatures are provided by two halogen lamps of 2KW each, one on the top and other at the bottom of the graphite holders. Helium is used as the ambient.

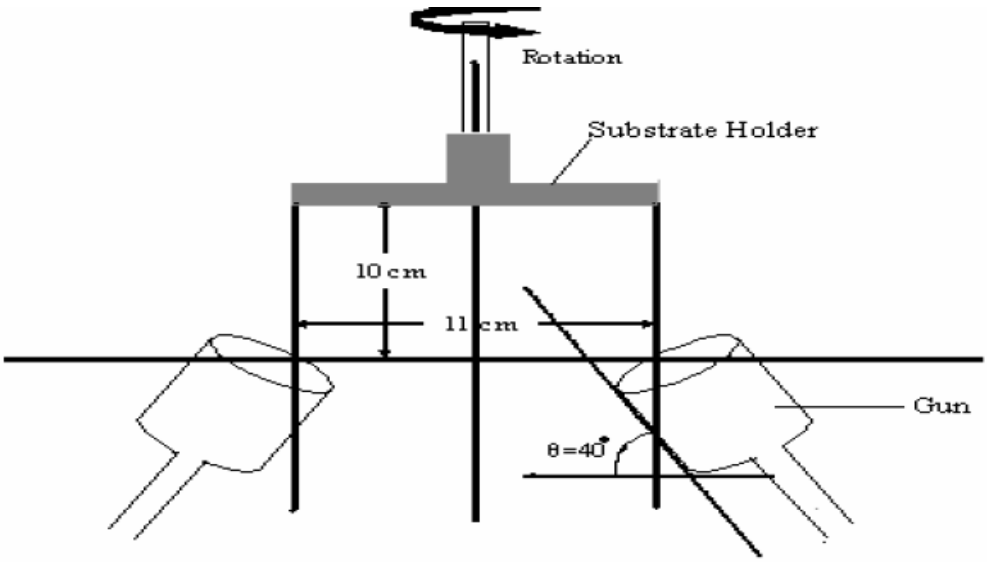

Figure 25. Schematic of sputter gun and substrate holder set-up [23]

4.1.4 Chemical bath deposition (CBD) of CdS

Cadmium sulphide is a commonly used semiconductor for optoelectronic devices. CdS films are deposited by several techniques including vacuum evaporation, spray pyrolysis, close spaced sublimation, electrodeposition, and precipitation from aqueous solutions. In

this work, CdS films are deposited from an aqueous solution. The solution growth process is based on the reaction of a cadmium salt, a complexing agent, and a sulphur compound in a heated aqueous solution. Cadmium acetate and Thiourea are used as sources of Cadmium and Sulphur respectively. Ammonium hydroxide, which is used as a complexing agent and ammonium acetate, which is used as buffer are combined in 600ml of water. The deposition set-up for CBD process is shown in figure 26. The substrates are placed in a 1000ml double jacketed beaker. The solution is maintained at a constant temperature of 85°C by circulating heated ethylene glycol through the hollow walls of the beaker. At regular time intervals, measured volumes of Sulphur and Cadmium precursors are added to the solution. A proposed mechanism was given by J.Herrero et al as follows.

$Cd(CH3COO)_2 \leftrightarrow Cd^{2+} + 2CH_3COO^-$

$NH_3 + HOH \leftrightarrow NH^{4+} + OH^-$

$Cd(NH3)_4^{2+} + 2OH^- \leftrightarrow [Cd(OH)_2(NH_3)_2] + 2NH_3$

$[Cd(OH)_2(NH_3)_2] + SC(NH_2)_2 \rightarrow [Cd(OH)_2(NH_3)_2SC(NH_2)_2]$

$[Cd(OH)_2(NH_3)_2SC(NH_2)_2] \rightarrow CdS_{(s)} + CN_3H_5 + NH_3 + 2HOH$

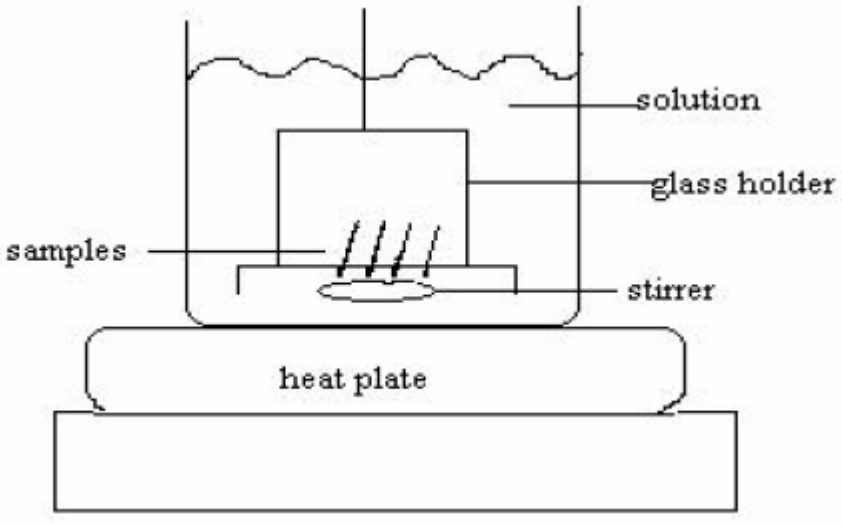

Figure 26. Chemical bath deposition set-up [23]

4.1.5 Close spaced sublimation of CdTe

CdTe absorber film is deposited on CdS/ZTO/SnO_2:F/glass film stack by the close spaced sublimation (CSS) technique. The deposition set-up for CSS is shown in figure 27. The substrates are annealed in H_2 at 400°C before CdTe deposition. The deposition is done at source temperatures of 680°C and substrate temperatures of 580°C to 600°C in a He/O_2 ambient. The spacing between the source and the substrate is 2 mm. Both source and substrate are heated using 2KW halogen lamps.

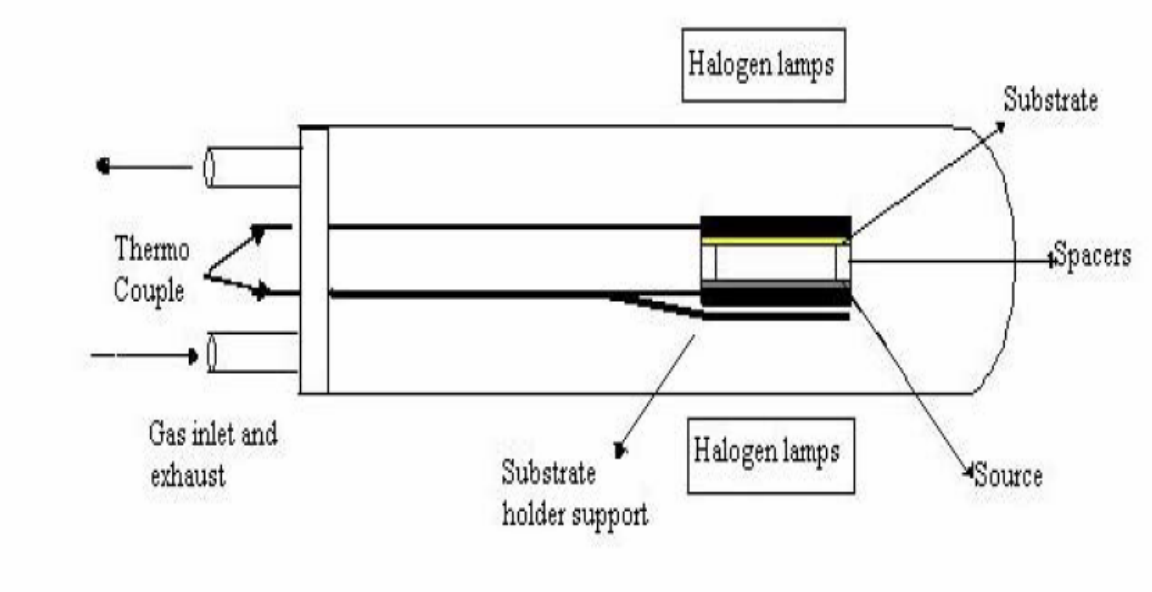

Figure 27. Schematic diagram of close spaced sublimation set-up [23]

4.1.6 Cadmium chloride heat treatment

After the CdTe deposition, a $CdCl_2$ heat treatment of the hetrojunction is essential to improve device performance. Cadmium chloride is evaporated from $CdCl_2$ pellets pressed from powder (99.999% purity) to a thickness of 8000Å at room temperature. Following the deposition, the samples are annealed in a He/O_2 ambient at 390°C for 25 minutes.

4.1.7 Contacting

The final step in the fabrication process of the cell is contacting. Graphite paste doped with HgTe:Cu is applied on the CdTe film, and then the substrates are annealed at 250°C in He ambient. The graphite contact is then coated with a thin conductive layer of silver. This completes the back contact of the solar cell. The CdTe around the cell is scraped exposing the TCO surface. Indium solder is applied to this exposed surface. This serves as a front metal contact, completing the fabrication of the CdS/CdTe solar cell. The basic device structure is shown in the figure 28.

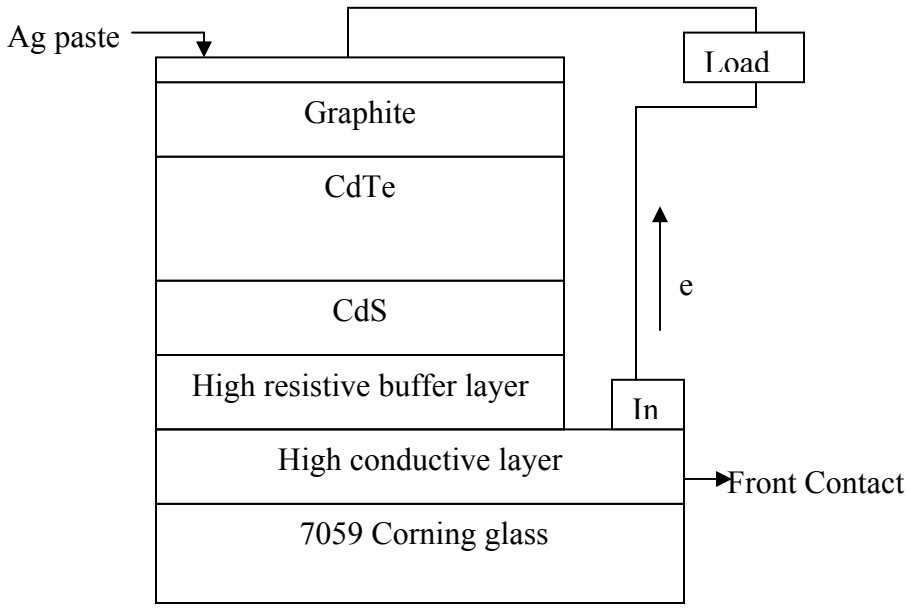

Figure 28. Standard device structure

4.2 Material & device characterization

4.2.1 Material characterization

Film characterization is carried out by various techniques. The thickness of the film is measured using a Tencor Alpha-step profilometer. The sheet resistance of the film

is measured using a simple four point probe set-up. The resistivity of the film is calculated using the thickness and sheet resistance values. Atomic composition is determined using a Tracor Northern (TN) 550 Energy Dispersive Spectrometer. Crystallinity and phase composition is determined using powder XRD. The surface topography and roughness of the films are studied using an Atomic Force Microscopy (Nanoscope Dimension 3000). For optical measurements, an Oriel Cornerstone monochromator (model 74100) with an integrating sphere is utilized.

4.2.2 Solar cell measurements

Light and dark I-V data is measured using a Keithley 2410 1100V source meter, keeping the cell under illumination from a solar simulator and covering the cell with a black cloth respectively. Open-circuit voltage (V_{OC}), fill factor (FF) and short-circuit current density (J_{SC}) are determined using a LABVIEW program used for data collection and processes. Quantum efficiency of the devices is measured using the Oriel Cornerstone monochromator (model 74100) with the support of another LABVIEW program used for operating the spectral response set-up. The light source used is a GE 400W/120V Quartz line lamp (model#43707).

CHAPTER 5

RESULTS AND DISCUSSION

5.1 Zn_2SnO_4 (Zinc stannate) films sputtered at room temperature

5.1.1 Structural and optical properties

Zn_2SnO_4 films are deposited by co-sputtering of SnO_2 and ZnO targets in Ar ambient at room temperature and at 400°C. Zn_2SnO_4 films are deposited on SnO_2:F /glass substrates. Figure 29 shows the X-ray diffraction (XRD) patterns of a room temperature deposited Zn_2SnO_4 film annealed at various temperatures. Table 5 shows the list of various materials appeared in the XRD patterns of room temperature deposited Zn_2SnO_4 films annealed at various temperatures. The peaks at approximate 2θ values of 26.15, 52.01, 54.47 and 66.19° are associated with the SnO_2:F. XRD analysis of the as-deposited film shows the peaks of the SnO_2:F layer. It also shows the emergence of $ZnSnO_3$ peaks. Subsequent annealing at higher temperatures in He ambient made these films polycrystalline. The films started to crystallize at 575°C. This is evident with the onset of the (311) peak corresponding to the spinel phase (Zn_2SnO_4) of the zinc stannate structure. Higher temperature annealing supplied the required energy for crystallization of these films. The preferred orientation is along [311] direction. The orthorhombic phase

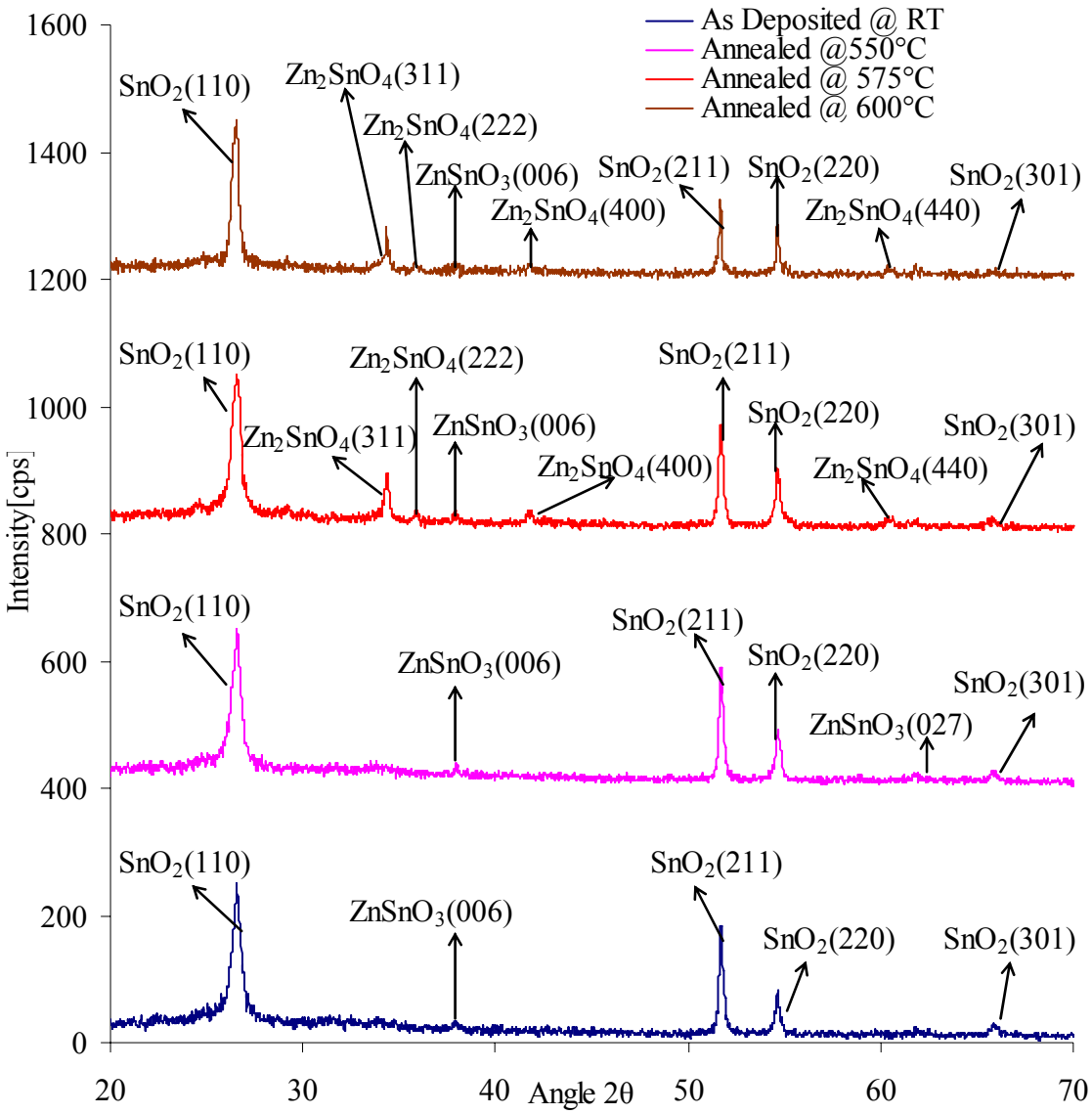

Figure 29. XRD of a room temperature deposited Zn_2SnO_4 annealed at various temperatures

Table 5. List of materials present in the XRD patterns of a room temperature deposited Zn_2SnO_4 film and annealed at various temperatures

ZTO HT [°C]	Zn_2SnO_4	$ZnSnO_3$	ZnO	SnO_2
As Deposited	NO	YES{(006)}	NO	NO
550°C	NO	YES{(006),(027)}	NO	NO
575°C	YES{(311),(222),(400),(440)}	YES{(006)}	NO	NO
600°C	YES{(311),(222),(400),(440)}	YES{(006)}	NO	NO

of zinc stannate ($ZnSnO_3$) is present in both the as-deposited and annealed films with no significant improvement in its intensity. No evidence of ZnO and SnO_2 related peaks in the Zn_2SnO_4 is observed.

Figure 30 shows the XRD pattern analysis of Zn_XSnO_Y films for X = 1.5, 1.9, 2.0, 2.1 and 2.5 annealed at 600°C. Table 6 shows the list of various materials appeared in the XRD patterns of room temperature deposited zinc stannate films with different Zn/Sn ratios. The peaks at approximate 2θ values of 26.15, 52.01, 54.47 and 66.19° are associated with the SnO_2:F. For X=1.5, there is no evidence of spinel (Zn_2SnO_4) phase of zinc stannate in the film. However, an emerging orthorhombic phase ($ZnSnO_3$) of zinc stannate is observed. At X value close to 2 and above (Zn rich), Zinc stannate films became crystalline in the spinel phase (Zn_2SnO_4) with preferred orientation along [311] direction. ZnO and SnO_2 related peaks are not observed in the films at all Zn/Sn ratios characterized.

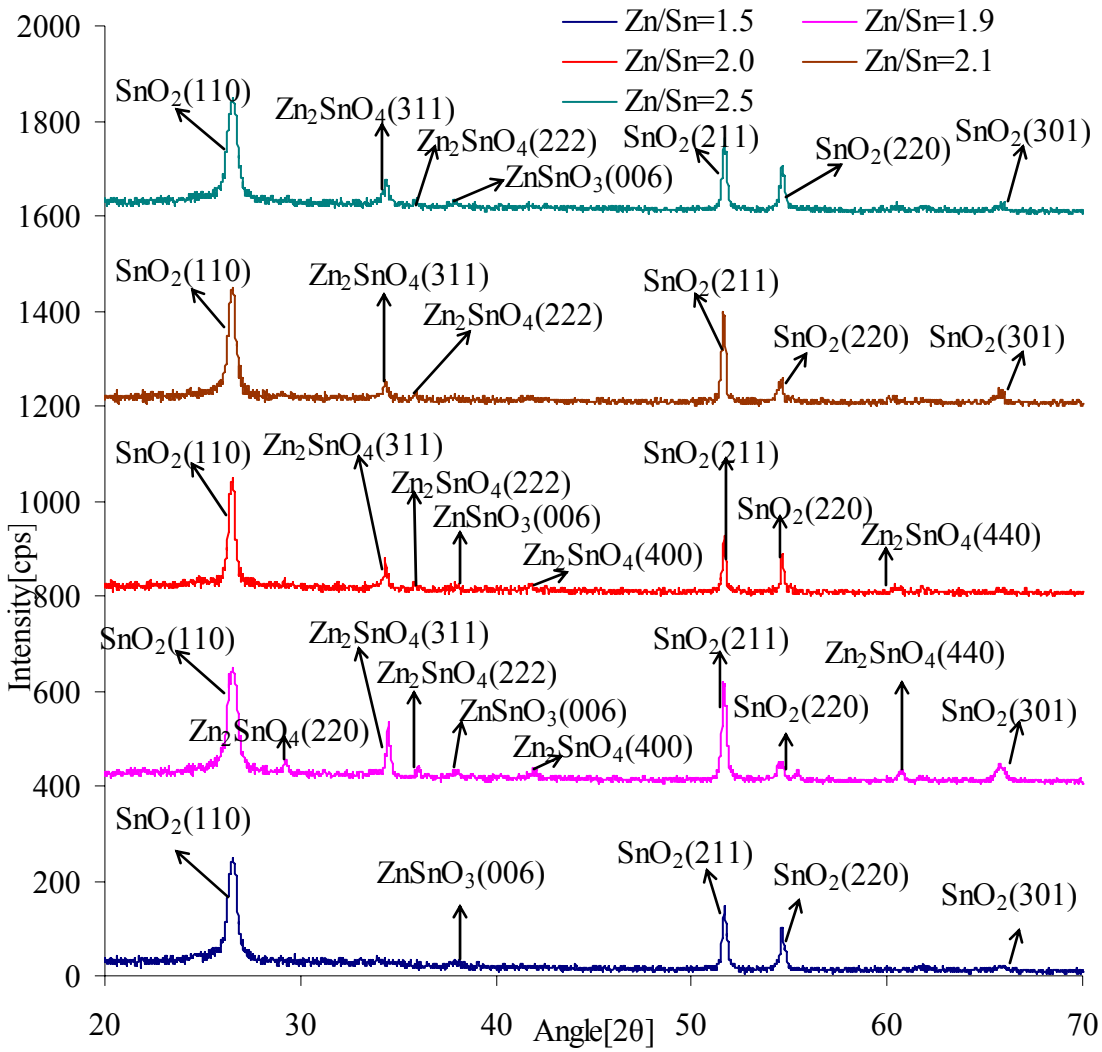

Figure 30. XRD of a room temperature deposited zinc stannate film with different Zn/Sn ratios

Table 6. List of materials present in the XRD patterns of room temperature deposited Zinc stannate films with different Zn/Sn ratios (Annealed at 600° C)

Zn/Sn	Zn_2SnO_4	$ZnSnO_3$	ZnO	SnO_2
1.5	NO	YES{(006)}	NO	NO
1.9	YES{(220),(311),(222),(400),(440)}	YES{(006)}	NO	NO
2.0	YES{(311),(222),(400),(440)}	YES{(006)}	NO	NO
2.1	YES{(311),(222)}	NO	NO	NO
2.5	YES{(311),(222)}	YES{(006)}	NO	NO

Figures 31 and 32 show the transmission spectra of the room temperature deposited ZTO films and subsequently annealed at different temperatures. The films are subjected to post deposition annealing at 575°C and 600°C in helium ambient. It is

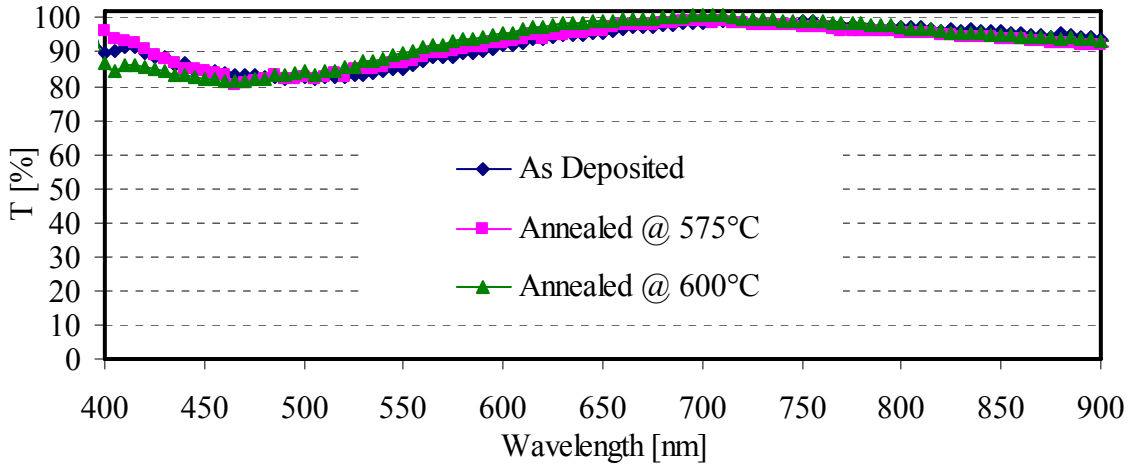

Figure 31. Transmission spectra of room temperature deposited Zn_2SnO_4 film and annealed at various temperatures

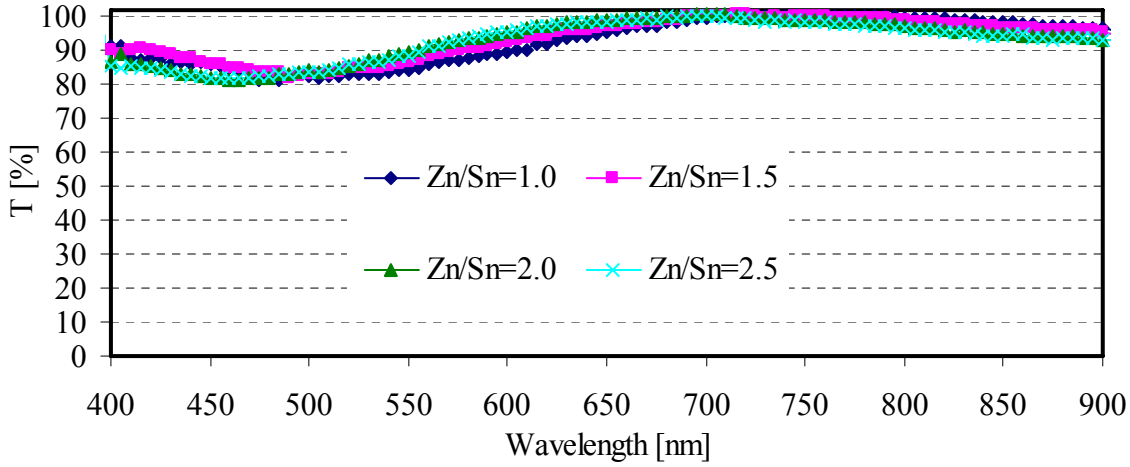

Figure 32. Transmission spectra of ZTO films with different Zn/Sn ratios [Annealed at 600°C]

evident from the transmission spectra shown in figure 31 that the films annealed at higher temperatures show a slight improvement possibly due to the increase in crystallinity. Figure 32 shows that the ZTO films with Zn/Sn=2.0 and Zn/Sn=2.5 are highly transparent. This is because the ZTO films with Zn/Sn ratios close to 2 became crystalline at higher temperatures while other films with Zn/Sn=1 and Zn/Sn=1.5 remained amorphous.

5.2 Zn_2SnO_4 (Zinc stannate) films sputtered at 400°C

5.2.1 Structural properties

Figure 33 compares the XRD analysis of Zn_2SnO_4 films deposited at 400°C with thicknesses 500Å, 750Å and 1250Å. Table 7 shows the list of various materials appeared in the XRD patterns of Zn_2SnO_4 films deposited at 400°C. Structural data shows that randomly oriented polycrystalline films are produced. Both the spinel phase and orthorhombic phase of zinc stannate film are observed. Zinc oxide related peak is observed in 500Å, 750Å films. The films are subsequently annealed at 600°C for 20 minutes. Figure 34 compares the XRD analysis of Zn_2SnO_4 films deposited at 400°C and annealed at 600°C for 20 minutes. Table 8 lists various materials appeared in the XRD patterns of Zn_2SnO_4 films deposited at 400°C and annealed at 600°C. Upon annealing of the films, the phases of zinc stannate appeared for the as-deposited zinc stannate is more pronounced and zinc oxide related peak is observed in all the films. Zinc stannate films deposited at room temperature crystallized in the inverse spinel structure and have shown no evidence of zinc oxide related peaks while the films deposited at 400°C strongly displayed the presence of orthorhombic phase ($ZnSnO_3$) and zinc oxide related peaks.

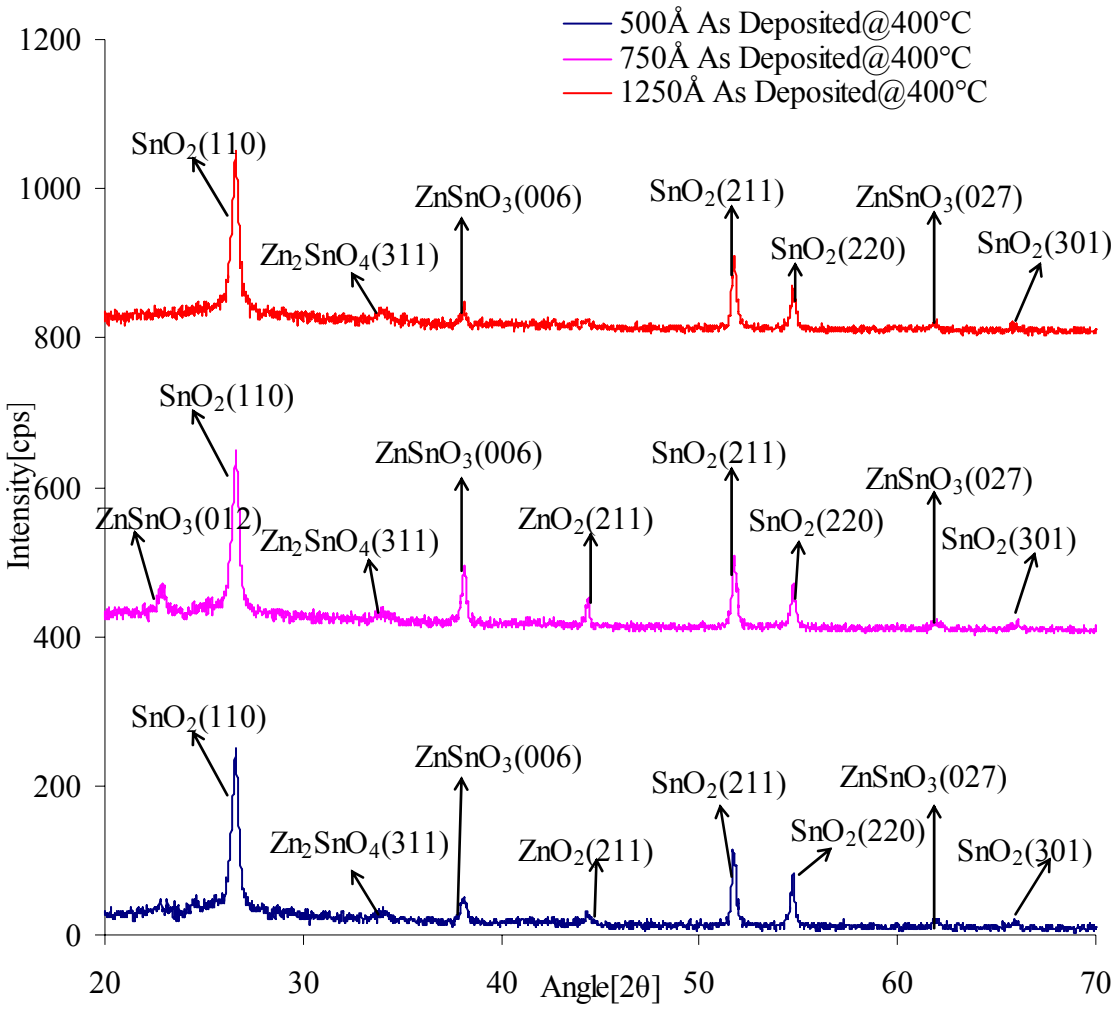

Figure 33. XRD of a 400°C deposited zinc stannate film

Table 7. List of materials present in the XRD patterns of Zn_2SnO_4 films deposited at 400°C

ZTO Thickness	Zn_2SnO_4	$ZnSnO_3$	ZnO	SnO_2
500Å	Possible{(311)}	YES{(006)}	YES{(211)ZnO_2}	NO
750Å	Possible{(311)}	YES{(012),(006),(027)}	YES{(211)ZnO_2}	NO
1250Å	Possible{(311)}	YES{(006),(027)}	NO	NO

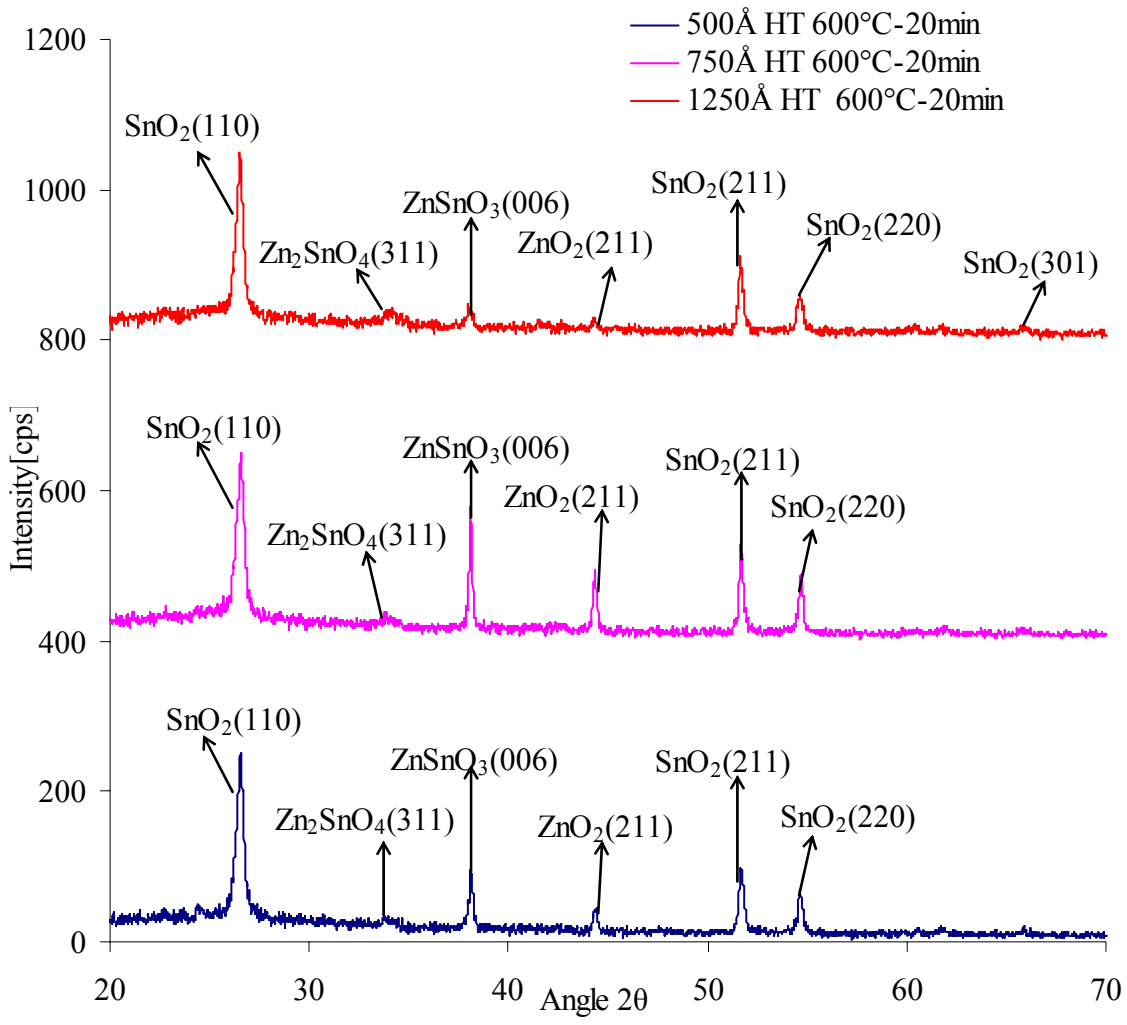

Figure 34. XRD of a 400°C deposited zinc stannate film and annealed at 600°C

Table 8. List of materials present in the XRD patterns of Zn_2SnO_4 films deposited at 400°C and annealed at 600°C

ZTO Thickness	Zn_2SnO_4	$ZnSnO_3$	ZnO	SnO_2
500Å	Possible	YES(006)	YES(211)ZnO_2	NO
750Å	YES(311)	YES(006)	YES(211)ZnO_2	NO
1250Å	Possible	YES(006)	YES(211)ZnO_2	NO

The surface of a 750Å thick zinc stannate film is analyzed using AFM. The AFM images of the as-deposited films at 400°C and annealed films are shown in figures 35 and 36 respectively. The scan size is 2µm. AFM measurements calculate the surface roughness for the as deposited ZTO film in argon ambient as 4.2 nm. Upon annealing the film at 600°C for 20 minutes in He made the surface rougher. The surface roughness of the annealed film is 5.3nm.

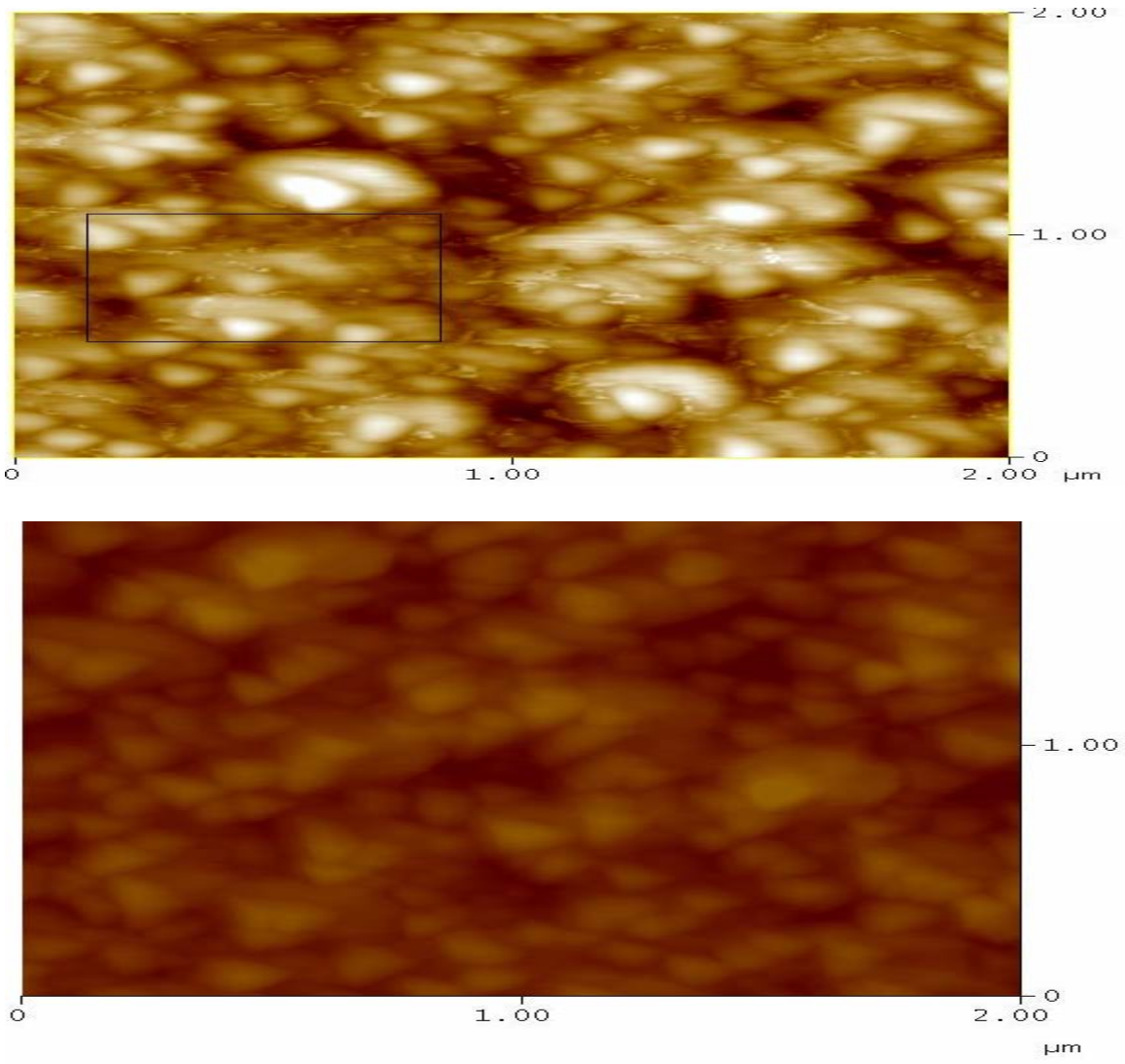

Figure 35. Two dimensional phase images of as-deposited ZTO film at 400°C (above) and annealed at 600°C for 20 minutes in He (below)

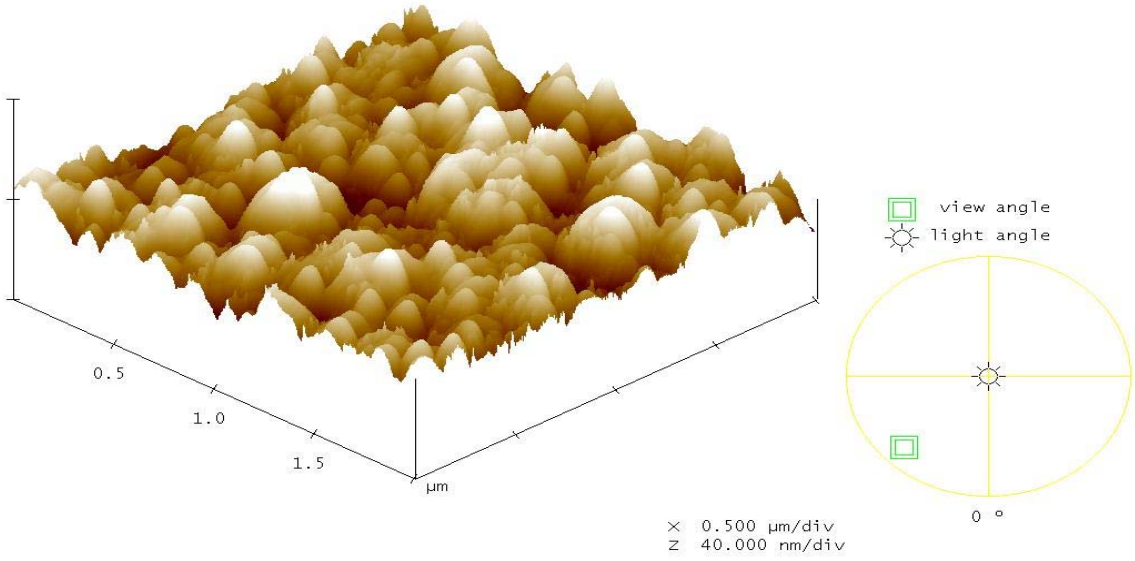

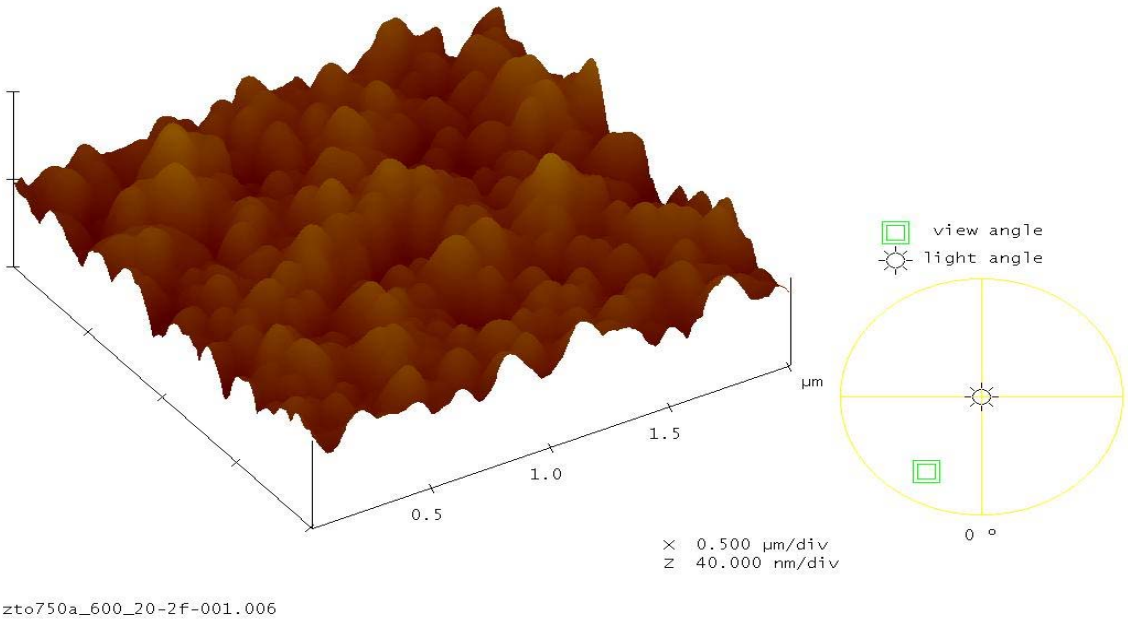

Figure 36. AFM images of ZTO film before (above) and after annealing (below)

5.3 CdS/CdTe solar cells using zinc stannate film as a buffer layer

5.3.1 Zinc stannate films sputtered at room temperature

As mentioned in the earlier chapter, the zinc stannate (ZTO) films are integrated as high resistive buffer layers in CdS/CdTe solar cells. ZTO films with a Zn/Sn=2.0 and film thickness of 2000Å is sputtered on SnO_2:F layer. This bilayer is subjected to a heat treatment at high temperatures ranging from 550°C to 600°C in He ambient for 20 minutes. This thin film is further processed to make a CdS/CdTe solar cell using standard processes.$CdCl_2$ heat treatment is done at 420°C for 15 minutes. The back contact used in this process is a Cu doped graphite paste. Table 9 shows the performance of a CdTe/CdS solar cell with 2000 Å Zn_2SnO_4 buffer layer.

Table 9. Summary of SnO_2:F/ Zn_2SnO_4 devices (ZTO room temperature deposited and Zn/Sn=2.0)

ZTO HT [°C]	V_{OC} [mV]	FF [%]	J_{SC} [mA/cm^2]	Efficiency [%]	R_{series} [Ω-cm^2]	R_{shunt} [Ω-cm^2]
550	730	55.4	23.8	9.34	1.90	950
575	680	54.4	23.4	8.66	1.90	530
600	780	58.2	24.5	11.13	2.34	800

5.3.1.1 J-V characteristics

The devices with SnO_2:F/ ZTO bilayer annealed at 600°C exhibited higher V_{OC}, FF and J_{SC} than the devices annealed at 550°C and 575°C. Nevertheless the V_{OC} and FF values for all the devices are lower than the typical CdTe/CdS solar cell values. Figure 37 shows the light J-V and dark J-V characteristics for SnO_2:F/ Zn_2SnO_4 devices. ZTO films

are deposited at room temperature and heat treated at 550°C, 575°C and 600°C. The observed trend may be due to the decrease in the shunt resistance of the devices. The dark

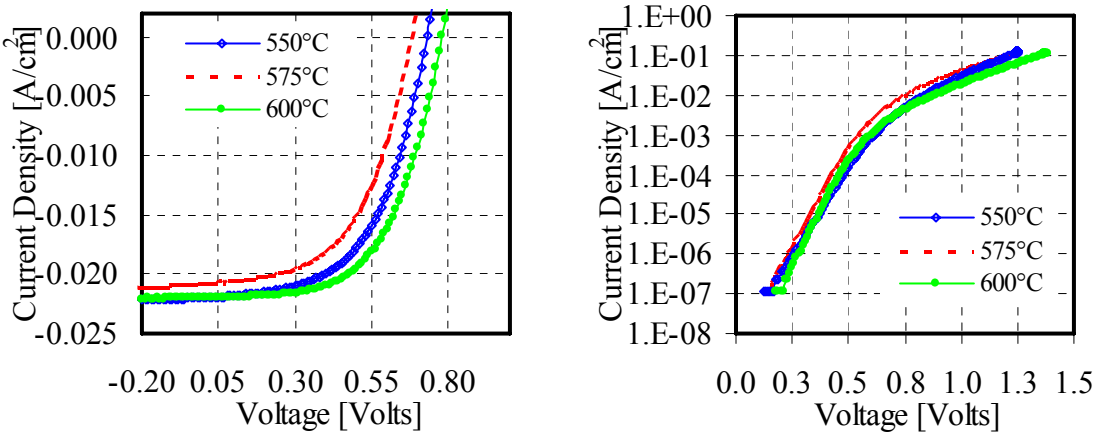

Figure 37. Light J-V (left) and dark J-V (right) characteristics for SnO_2:F/ Zn_2SnO_4 devices (ZTO room temperature deposited and Zn/Sn=2.0)

currents of all the devices are higher but the device with ZTO film annealed at 600°C has lower dark current compared to other two devices.

5.3.1.2 Spectral response

It is evident from the spectral response data of figure 38 that the devices displayed differences in the current generation. This difference is mainly pronounced for the wavelengths below 550nm. The device with annealed bilayer at 600°C has higher current generation below 550nm. This might be due to the high degree crystalline nature of the zinc stannate film annealed at high temperatures. The thinner CdS for films annealed at higher temperatures suggest that the interdiffusion phenomenon between zinc stannate and CdS has consumed more CdS in this case compared to other temperature annealed

films [20]. This result seems counterintuitive as one might expect more interdiffusion with amorphous zinc stannate film. This thinner CdS has reduced the amount of light

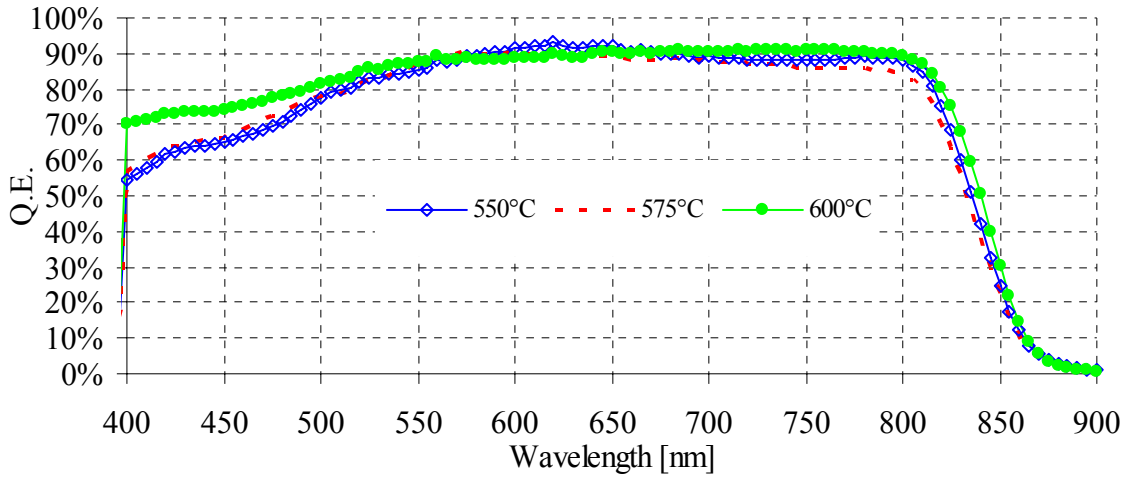

Figure 38. Spectral response graph for SnO_2:F/ Zn_2SnO_4 devices (ZTO deposited at room temperature and Zn/Sn=2.0)

absorbing in the CdS region there by allowing the light to be absorbed in the CdTe absorber region which led to the higher quantum efficiency in the blue region of the spectrum.

5.3.2 Zinc stannate films sputtered at room temperature with varying Zn/Sn ratios

The effect of stoichiometry of the zinc stannate buffer layer on the performance of solar cells is studied by varying Zn/Sn ratio in the zinc stannate film. Solar cells are made using the zinc stannate films with Zn/Sn =1.5, 1.9, 2.0, 2.1 and 2.5. The zinc stannate film is sputtered on SnO_2: F layer at room temperature in Ar ambient and later annealed in He at 600°C for 20 minutes. Table 10 shows the performance of CdTe/CdS solar cells with 2000Å ZTO buffer layer. The ZTO film is deposited at room temperature and heat treated at 600°C. $CdCl_2$ heat treatment is done at 420°C for 15 minutes.

Table 10. Summary of SnO_2:F/ Zinc stannate devices (ZTO room temperature deposited and Zn/Sn=1.5, 1.9, 2.0, 2.1 and 2.5)

Zn/Sn	V_{OC} [mV]	FF [%]	J_{SC} [mA/cm^2]	Efficiency [%]	R_{series} [Ω-cm^2]	R_{shunt} [Ω-cm^2]
1.5	710	54.6	24.4	9.45	2.32	500
1.9	770	44.3	24	8.17	2.34	730
2.0	780	58.2	24.5	11.13	2.30	800
2.1	810	66.6	23.1	12.43	2.47	800
2.5	790	66.7	23	12.12	1.39	900

5.3.2.1 J-V characteristics

Figure 39 shows the light J-V and dark J-V characteristics for SnO_2:F/Zinc stannate devices with various Zn/Sn ratios. The devices with Zn/Sn ratios of 2.0 and above have shown better performance in terms of V_{OC}'s and FF's. The shunt resistances of all the devices are low. The dark currents are higher for all the devices. Dark J-V characteristics

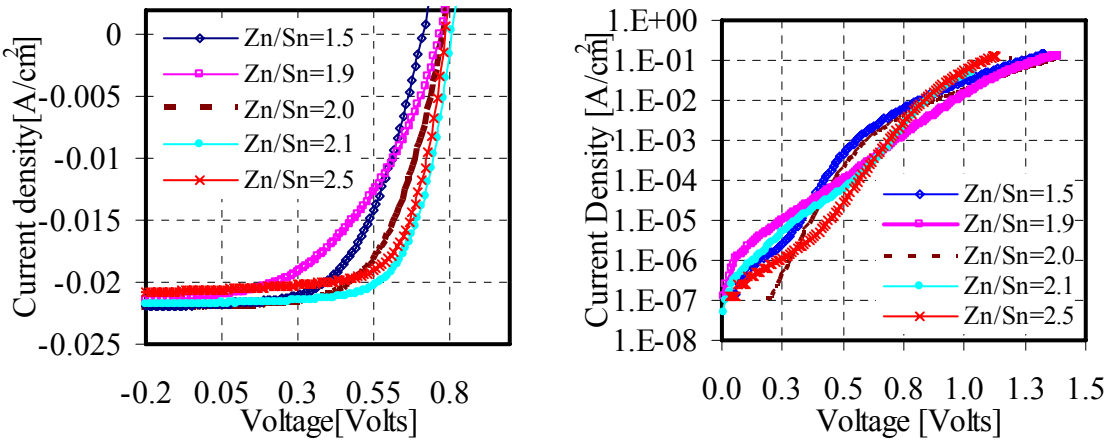

Figure 39. Light J-V (left) and dark J-V (right) characteristics of SnO_2:F/ Zinc stannate devices (ZTO room temperature deposited and Zn/Sn=1.5, 1.9, 2.0, 2.1 and 2.5)

are inconclusive to determine the effect of Zn/Sn ratio on the solar cell performance.

5.3.2.2 Spectral response

The spectral response data from figure 40 showed clear difference in the quantum efficiency of the devices below 550nm. This quantum efficiency data suggests that the CdS has been entirely consumed in the devices with Zn/Sn ratios less than 2.0 during the fabrication process. The device with Zn/Sn=1.9 suffered from poor collection at longer wavelengths.

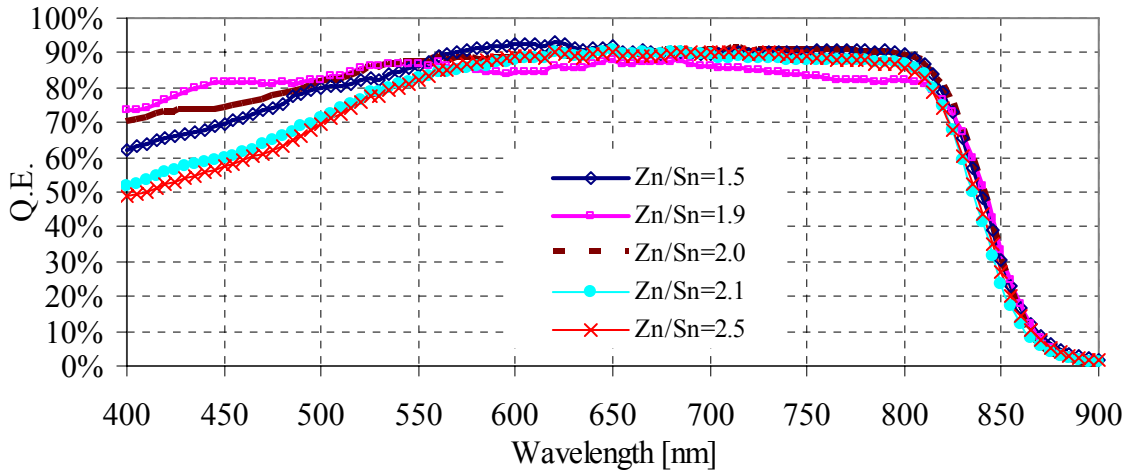

Figure 40. Spectral response of SnO_2:F/ Zinc stannate devices (ZTO room temperature deposited and Zn/Sn=1.5, 1.9, 2.0, 2.1 and 2.5)

5.3.2.3 Collection issues

For all the devices, monochromatic J-V data is collected and analyzed to develop an insight to the specific collection mechanism. The monochromatic J-V graphs are shown in figure 41. The conditions for each set of graphs are inserted in the text box. The FF vs Wavelength graphs for each condition are also included in figure 41 adjacent to the monochromatic J-V. The dotted line indicates the FF. The device with Zn/Sn=1.5 has low R_{shunt} at all wavelengths. At 800nm, this device has poor collection. The device with Zn/Sn=1.9 has high monochromatic FF's than the white light FF. This device suffers

from high series resistance effect for all wavelengths. Higher series resistance effect is also obvious for the devices with Zn/Sn=2.0.

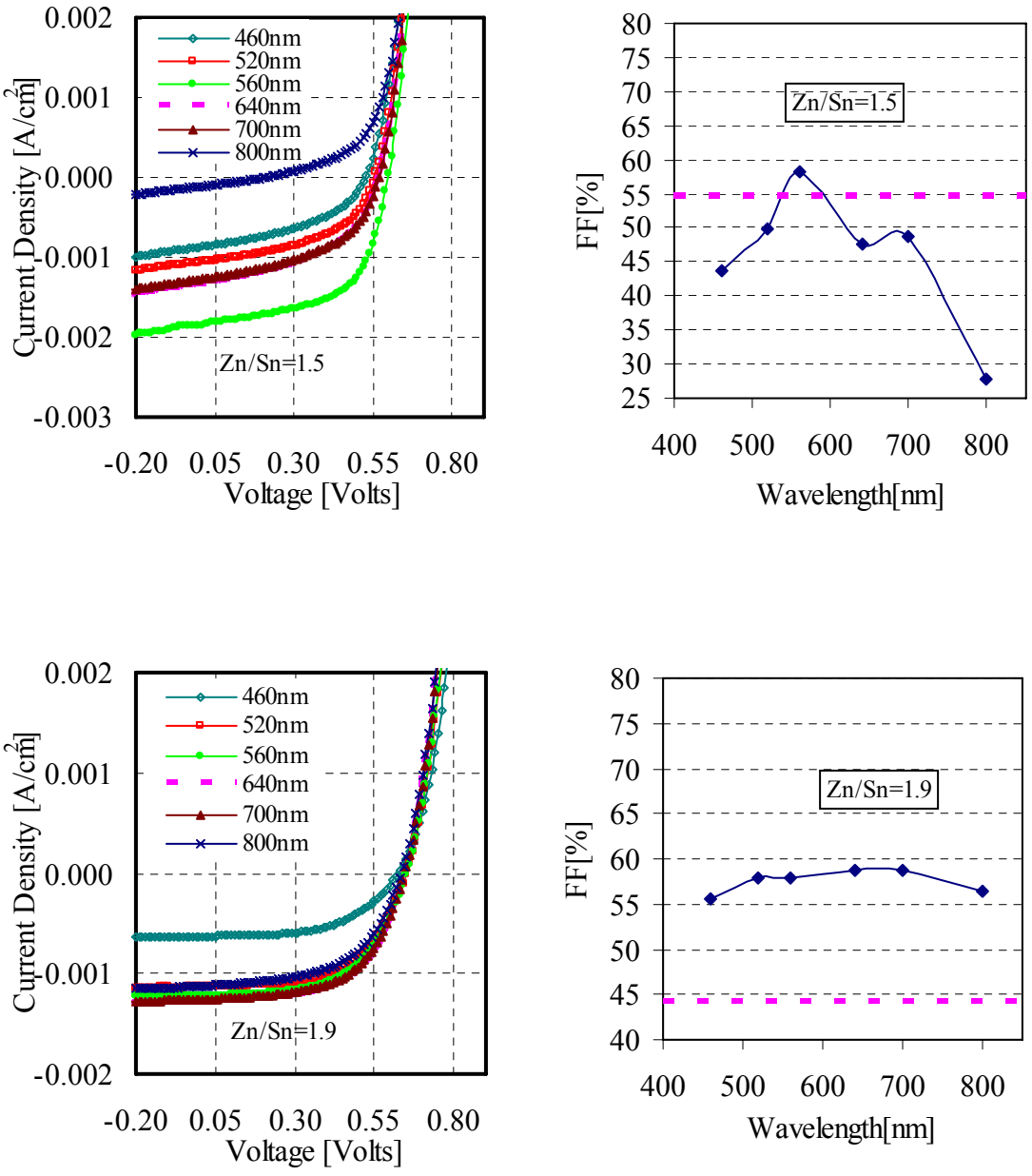

Figure 41. Monochromatic I-V curves and FF vs. wavelength plots for SnO_2:F/ Zinc stannate devices (ZTO room temperature deposited and Zn/Sn=1.5, 1.9, 2.0, 2.1 and 2.5)

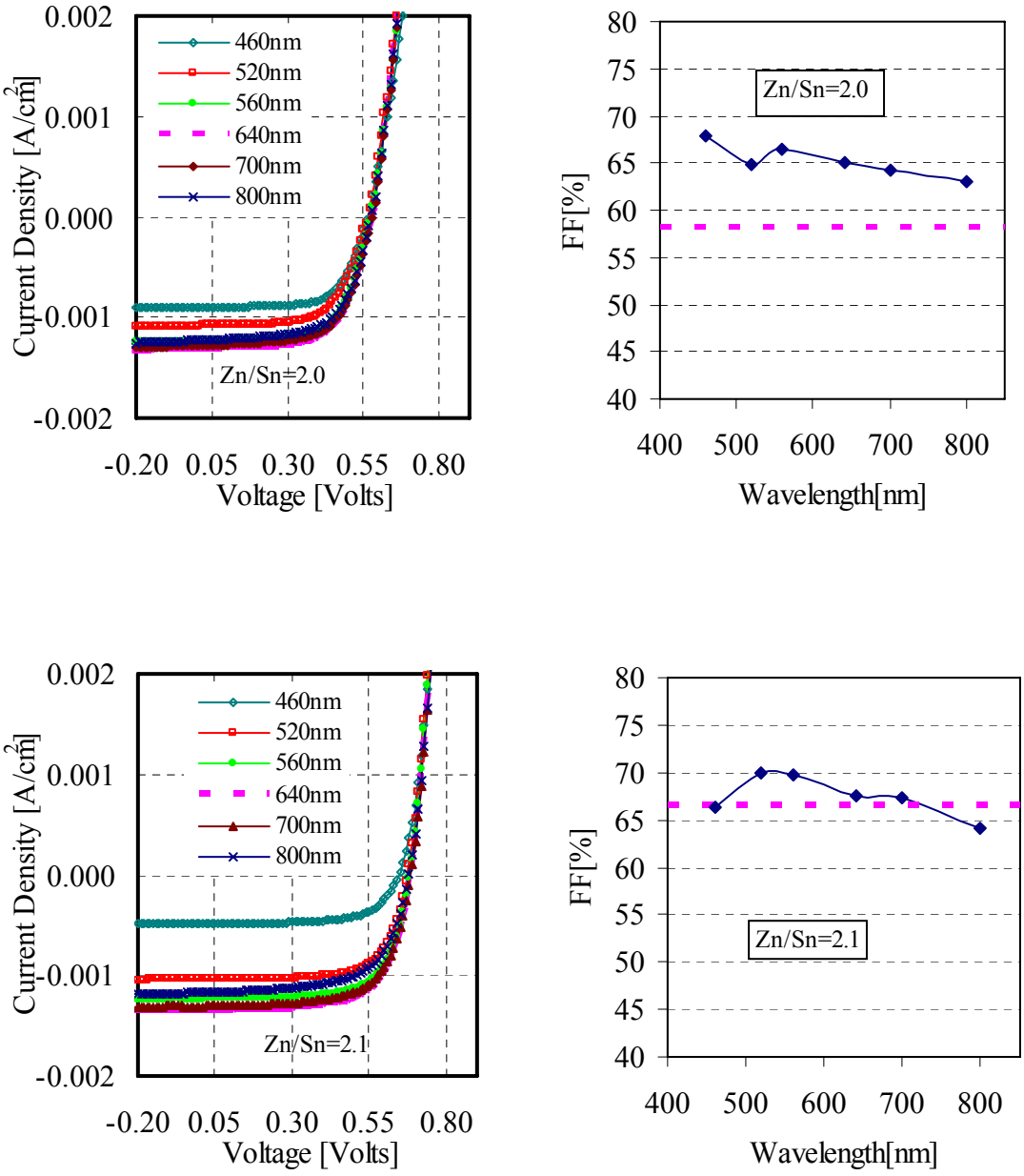

Figure 41. (Continued)

5.3.3 Zinc stannate films sputtered at 400°C

Zinc stannate films are deposited at 400°C in Ar ambient for three different thicknesses, 500Å, 750Å and 1250Å. The films are subsequently annealed at 600°C for 5, 20 and 30

minutes in He ambient. For all the devices, the $CdCl_2$ heat treatment was carried out in same conditions.

5.3.3.1 Zinc stannate films annealed at 600°C for 5 minutes

The results for the cells processed with ZTO sputtered at 400°C and annealed at 600°C for 5 minutes are listed in table 11.

Table 11. Summary of SnO_2:F/ Zinc stannate devices (ZTO sputtered @ 400°C and Zn/Sn= 2.0, annealed @ 600°C for 5 min)

ZTO thickness [Å]	V_{OC} [mV]	FF [%]	J_{SC} [mA/cm^2]	Efficiency [%]	R_{series} [Ω-cm^2]	R_{shunt} [Ω-cm^2]
500	840	68.2	24.40	13.98	1.64	1700
750	830	68.2	24.84	14.04	1.75	1900
1250	820	69.1	24.39	13.83	1.47	2000

5.3.3.1.1 J-V characteristics

Figure 39 shows the light J-V and dark J-V characteristics for SnO_2:F/ Zn_2SnO_4 devices with ZTO deposited at 400°C and annealed at 600°C for 5 minutes. All the devices showed improved performance in all aspects compared to the devices made with room temperature deposited ZTO films. The R_{shunt} for all the devices with ZTO deposited at 400°C is much higher than that of the devices with room temperature deposited ZTO. The XRD data of ZTO films deposited at 400°C showed the presence of zinc oxide (ZnO_2) which may be the reason for improved R_{shunt} in these devices. The 500Å and 750Å zinc stannate films showed similar performance.

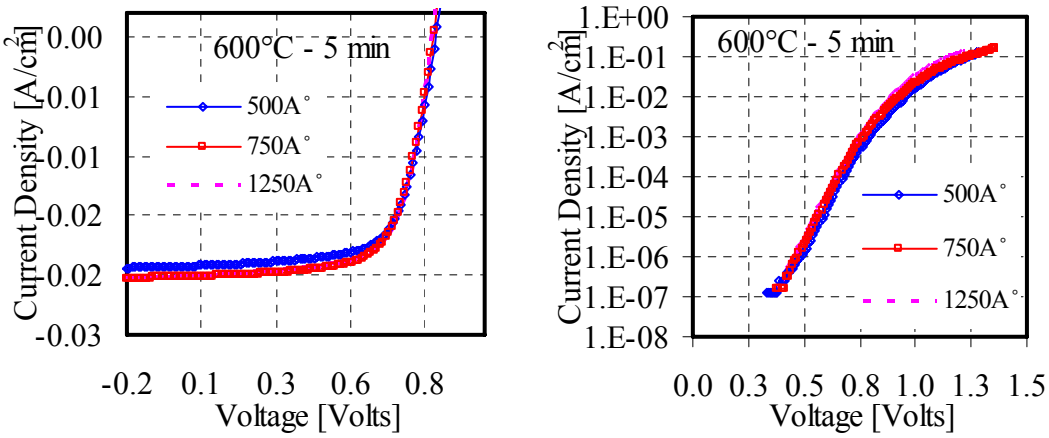

Figure 42. Light J-V (left) and dark J-V (right) characteristics of SnO_2:F/ Zinc stannate devices (ZTO sputtered @ 400°C and Zn/Sn= 2.0, annealed @ 600°C for 5 min)

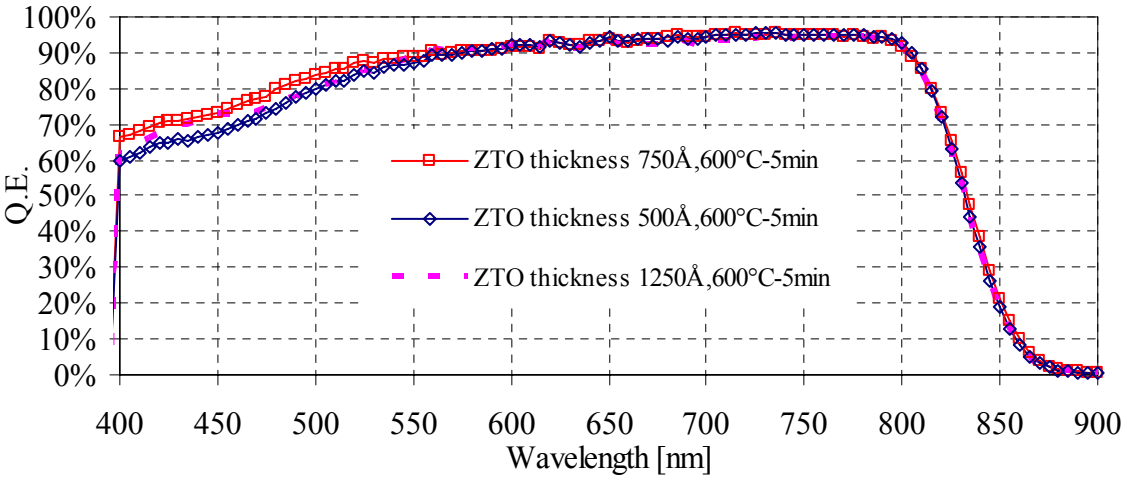

Figure 43. Spectral response of SnO_2:F/ Zinc stannate devices (ZTO sputtered @ 400°C and Zn/Sn= 2.0, annealed @ 600°C for 5 min)

5.3.3.1.2 Spectral response

The spectral response data of all the devices as shown in figure 43 is similar at all wavelengths above 550nm.The differences in the spectral response below 550nm can be contributed to the amount of CdS consumed during the fabrication process. The CdS seems to have been thinned by the ZTO with little impact on the V_{OC} of the device. The

CdS is thinner for the device with 750Å ZTO film. The thinner CdS allows for a greater current collection at lower wavelengths. Increase in the quantum efficiency of all devices above 600nm is observed.

5.3.3.1.3 Collection issues

For all the devices, the monochromatic J-V graphs are shown in the figure 44. The conditions for each set of graphs are inserted in the text box. The FF vs Wavelength graphs for each condition are also included in figure 44 adjacent to the monochromatic J-V. The dotted line indicates the white light FF. The devices with larger zinc stannate thickness i.e. 750Å and 1250Å have higher current at 460nm. All the devices showed good collection at longer wavelengths ranging from 600nm to 800nm.

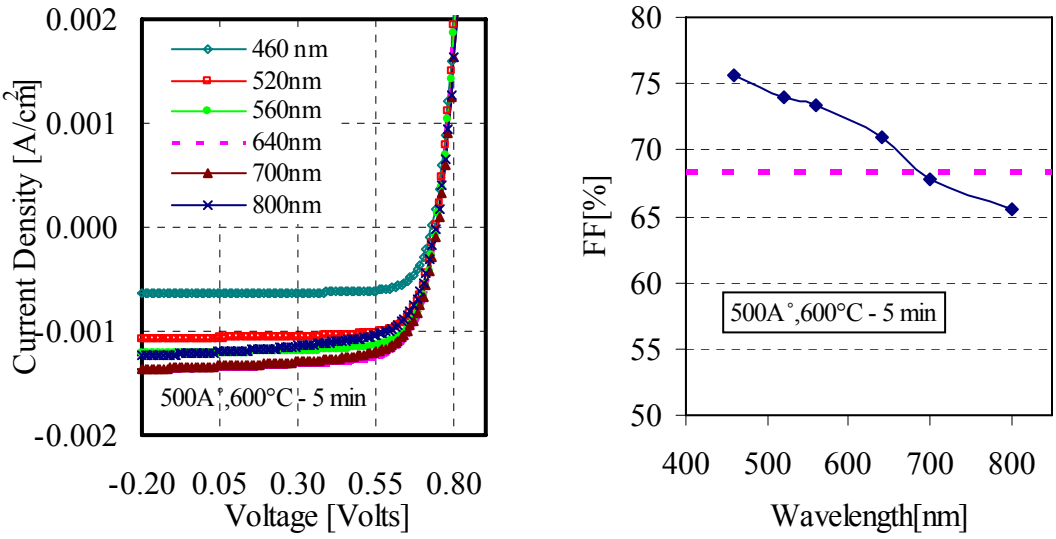

Figure 44. Monochromatic I-V curves and fill factor vs. wavelength plots for SnO_2:F/ Zinc stannate devices (ZTO sputtered @ 400°C and Zn/Sn= 2.0, annealed @ 600°C for 5 min)

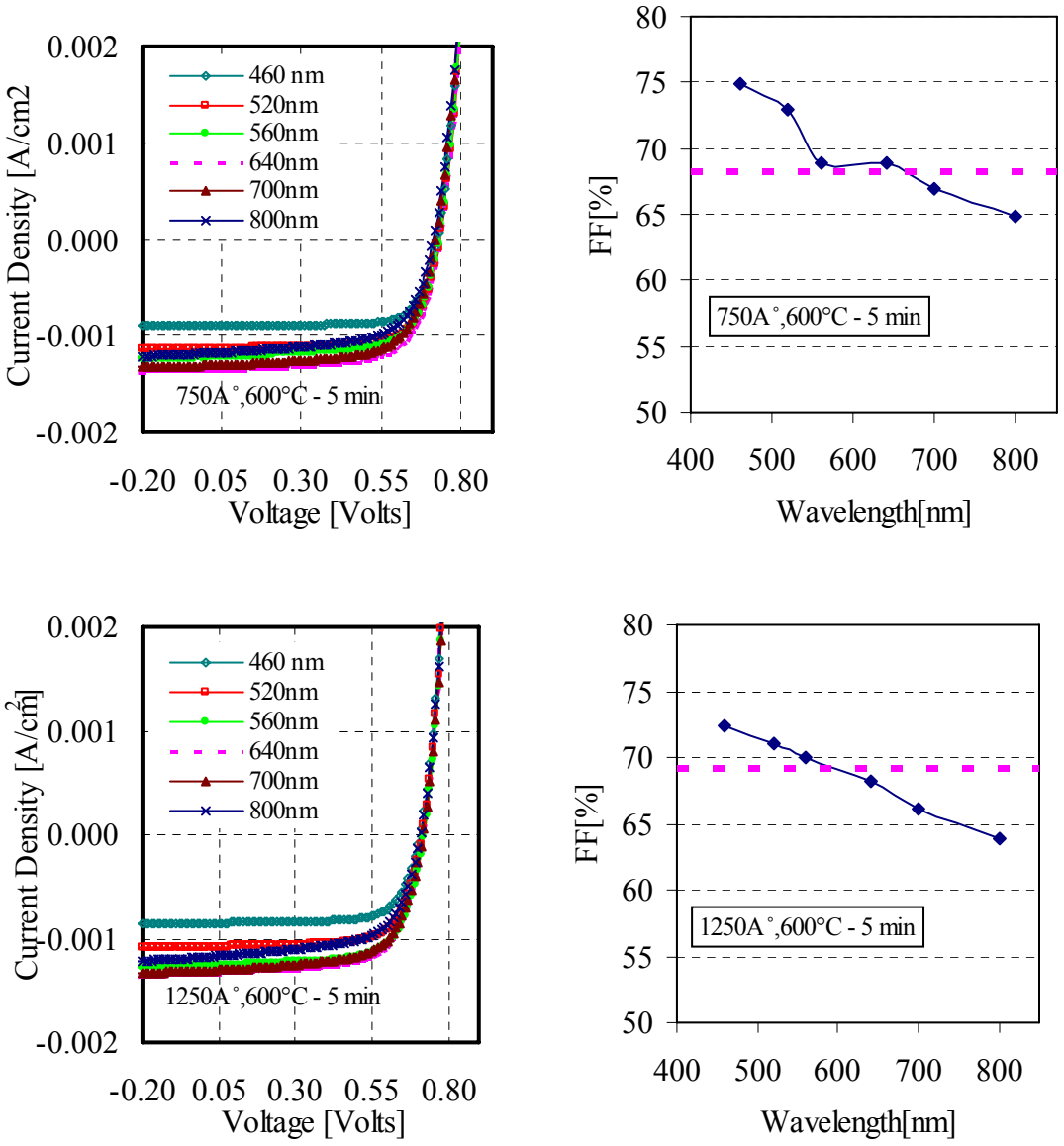

Figure 44. (Continued)

5.3.3.2 Zinc stannate films annealed at 600°C for 20 minutes

The results for the cells processed with ZTO sputtered at 400°C and annealed at 600°C for 20 minutes are listed in table 12.

Table 12. Summary of SnO_2:F/ Zinc stannate devices (ZTO sputtered @ 400°C and Zn/Sn= 2.0, annealed @ 600°C for 20 min)

ZTO thickness [Å]	V_{OC} [mV]	FF [%]	J_{SC} [mA/cm^2]	Efficiency [%]	R_{series} [Ω-cm^2]	R_{shunt} [Ω-cm^2]
500	830	70.8	23.8	13.99	1.44	1730
750	820	69.2	24.3	13.79	1.26	1700
1250	610	61.2	22.8	8.51	1.91	1000

5.3.3.2.1 J-V characteristics

Figure 45 shows the light J-V and dark J-V characteristics for SnO_2:F/ Zn_2SnO_4 devices with ZTO deposited at 400°C and annealed at 600°C for 20 minutes. The devices with ZTO film thickness 500Å and 750Å showed similar performance. The presence of zinc oxide in the ZTO films improved the shunt resistance of the devices. The degraded performance of the device with 1250 Å thick ZTO must have been an anomaly in the device processing and cannot be attributed to the ZTO buffer layer. It suffered from high dark currents.

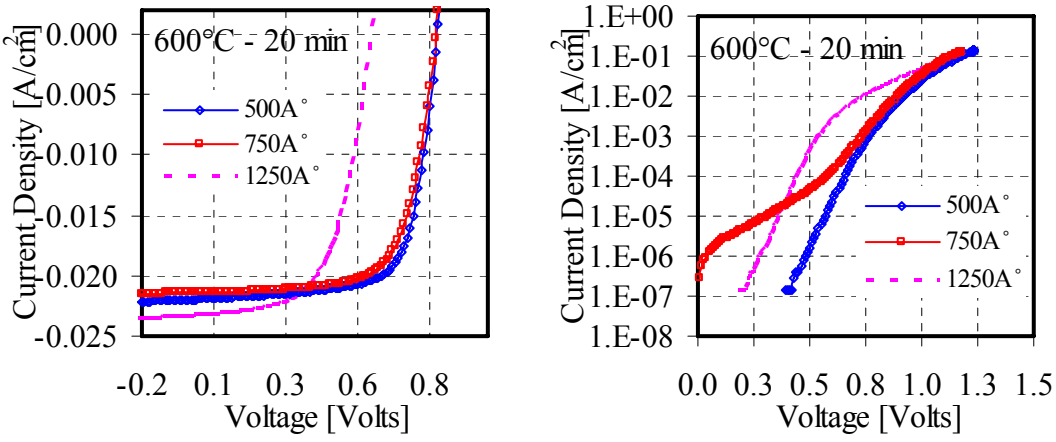

Figure 45. Light J-V (left) and dark J-V (right) characteristics of SnO_2:F/ Zinc stannate devices (ZTO sputtered @ 400°C and Zn/Sn= 2.0, annealed @ 600°C for 20 minutes)

5.3.3.2.2 Spectral response

The spectral response of the devices is shown in figure 46.The device with 750Å thick ZTO has higher quantum efficiency below 550nm. The device with 500Å thick ZTO annealed at 600°C for 20 minutes behaved similarly with the one annealed at 600°C for 5 minutes. But the longer wavelength quantum efficiency ranging from 600nm to 800nm is low for this set of devices compared to the ones annealed at 600°C for 5 minutes. This may be due to the poor collection in that region.

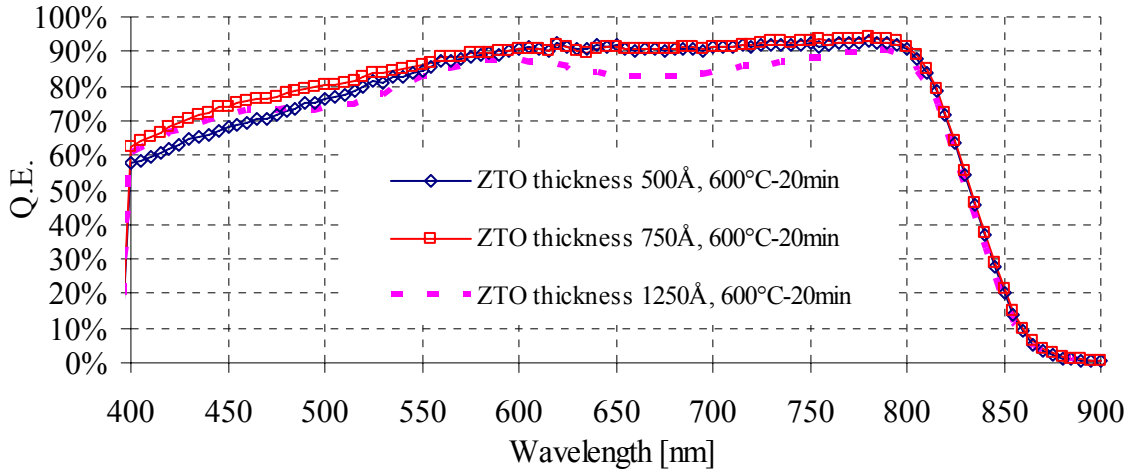

Figure 46. Spectral response of SnO_2:F/ Zinc stannate devices (ZTO sputtered @ 400°C and Zn/Sn= 2.0, annealed @ 600°C for 20 min)

5.3.3.3 Zinc stannate films annealed at 600°C for 30 minutes

The results for the cells processed with ZTO sputtered at 400°C and annealed at 600°C for 30 minutes are listed in table 13.

Table 13. Summary of SnO_2:F/ Zinc stannate devices (ZTO sputtered @ 400°C and Zn/Sn = 2.0, annealed @ 600°C for 30 min)

ZTO Thickness [Å]	V_{OC} [mV]	FF [%]	J_{SC} [mA/cm^2]	Efficiency[%]	R_{series} [Ω-cm^2]	R_{shunt} [Ω-cm^2]
500	830	69.3	24.74	14.21	1.33	1900
750	820	70.1	22.8	13.11	1.25	1890
1250	660	61.6	23.1	9.40	2.25	1200

5.3.3.3.1 J-V characteristics

Figure 47 shows the light J-V and dark J-V characteristics for SnO_2:F/ Zn_2SnO_4 devices with ZTO deposited at 400°C and annealed at 600°C for 30 minutes. The devices with zinc stannate film thickness 500Å and 750Å showed similar performance in terms of V_{OC} and FF's. The presence of zinc oxide in the ZTO films improved the shunt resistance of the devices. The series resistance of the device with 1250Å thick zinc stannate film is also higher compared to other devices in this set.

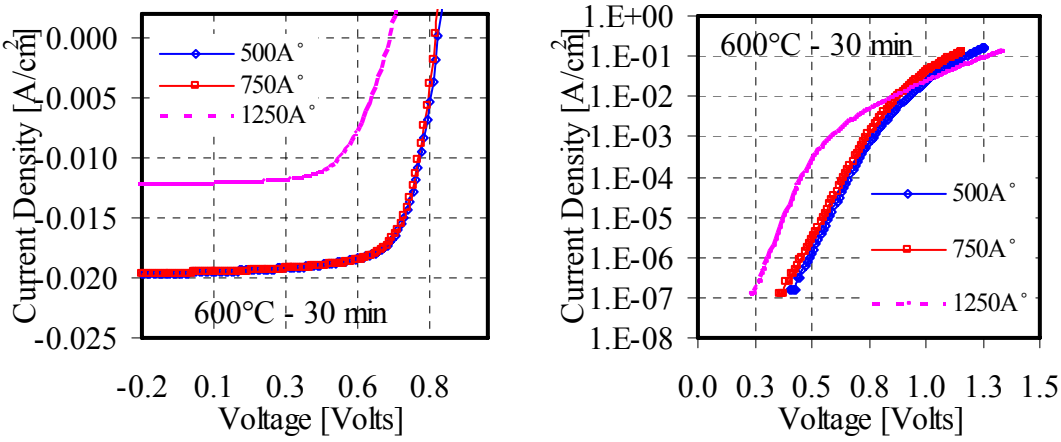

Figure 47. Light J-V (left) and dark J-V (right) curves of SnO_2:F/ Zinc stannate devices (ZTO sputtered @ 400°C and Zn/Sn= 2.0, annealed @ 600°C for 30 min)

5.3.3.3.2 Spectral response

The spectral response data from figure 48 shows that the quantum efficiency of the device with 500Å thick zinc stannate film has high quantum efficiency at all wavelengths. The quantum efficiency of the devices with 750A˚ and 1250A˚ thick zinc stannate films has a drop at longer wavelengths ranging from 600nm to 800nm. This may be due to the poor collection in the devices.

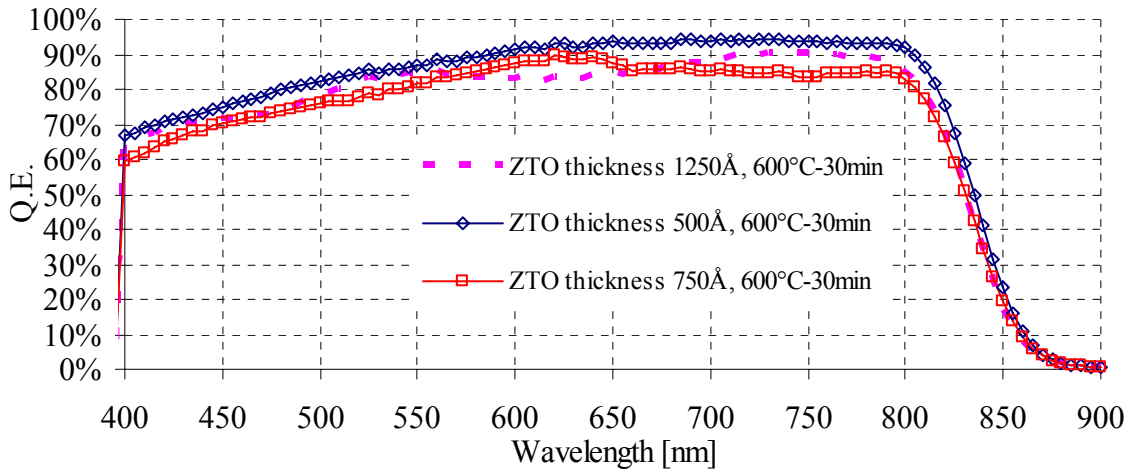

Figure 48. Spectral response of SnO_2:F/ Zinc stannate devices (ZTO sputtered @ 400°C and Zn/Sn= 2.0, annealed @ 600°C for 30 min)

5.3.3.3.3 Collection issues

The monochromatic J-V graphs are shown in the figure 49. The conditions for each set of graphs are inserted in the text box. The FF vs Wavelength graphs for each condition are also included in figure 49 adjacent to the monochromatic J-V. The dotted line indicates the white light FF. The device with 1250Å thick zinc stannate film has higher monochromatic FF's than the white light FF. This device suffers from high series resistance effect for all wavelengths. This led to the decrease in the fill factor of the device.

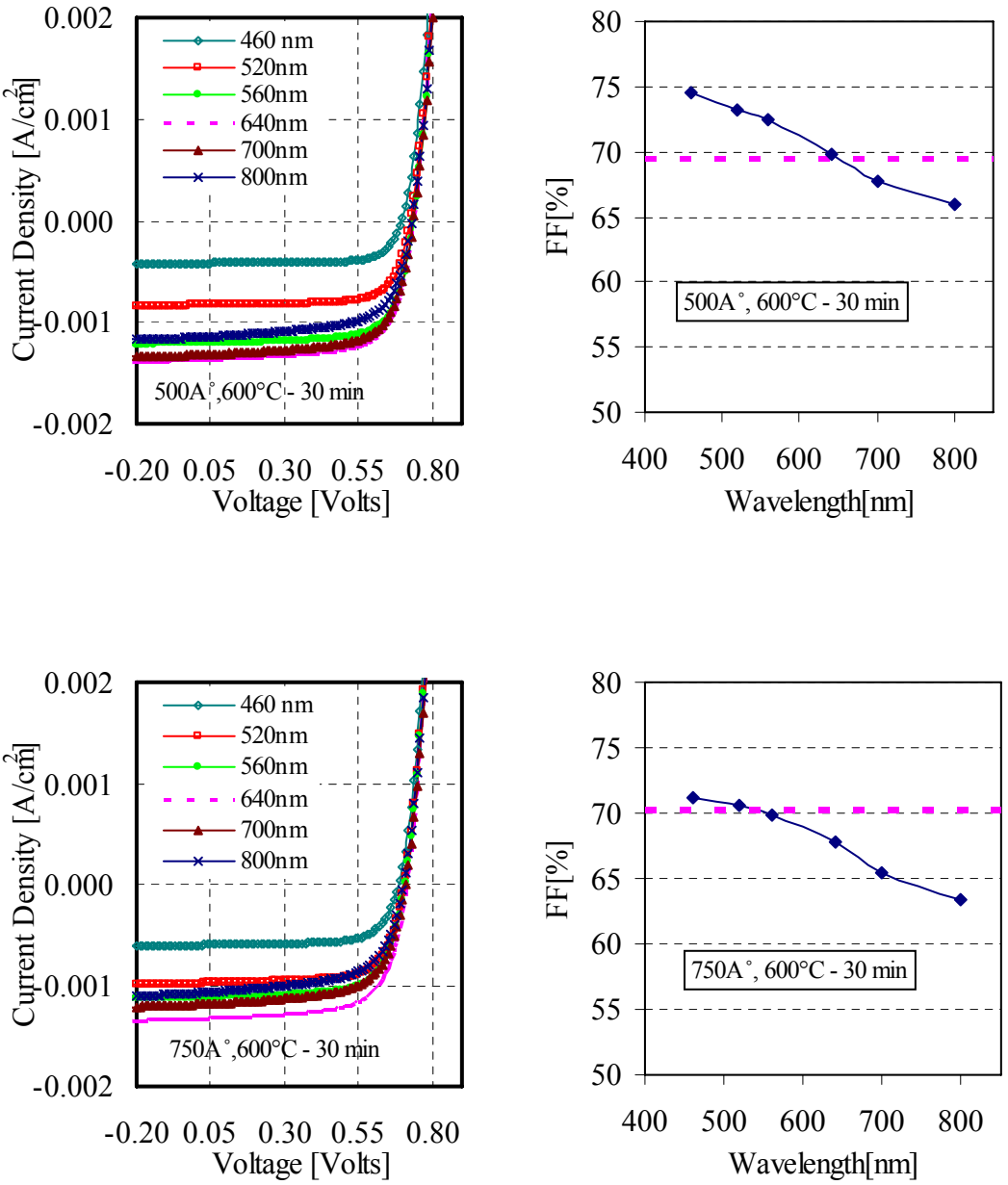

Figure 49. Monochromatic J-V curves and fill factor vs. wavelength plots for SnO_2:F/ Zinc stannate devices (ZTO sputtered @ 450°C and Zn/Sn= 2.0, annealed @ 600°C for 30 min)

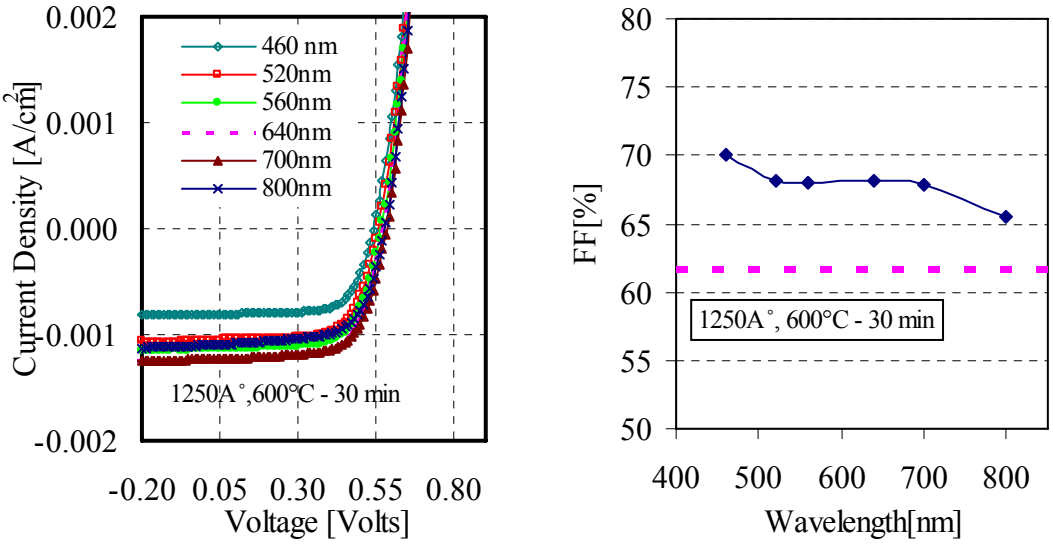

Figure 49. (Continued)

5.4 Highly conductive transparent conducting oxides

5.4.1 Cadmium stannate

5.4.1.1 Structural and optical properties

Cadmium stannate films are deposited by co-sputtering of SnO_2 and CdO targets in Ar ambient at room temperature. As-deposited films are amorphous in nature. As-deposited films can be made polycrystalline by subjecting them to high temperature annealing in He ambient. Cd_2SnO_4 begins to crystallize at approximately 525°C [22]. Figure 50 shows the XRD patterns of Cd_2SnO_4 films annealed at four different temperatures. The films turned crystalline with a preferred orientation in the [222] direction. At all the annealing temperatures, films crystallized in single phase of Cd_2SnO_4. There is no evidence of secondary phases of $CdSnO_3$, SnO_2 and CdO in the films. This shows that Cd_2SnO_4 films

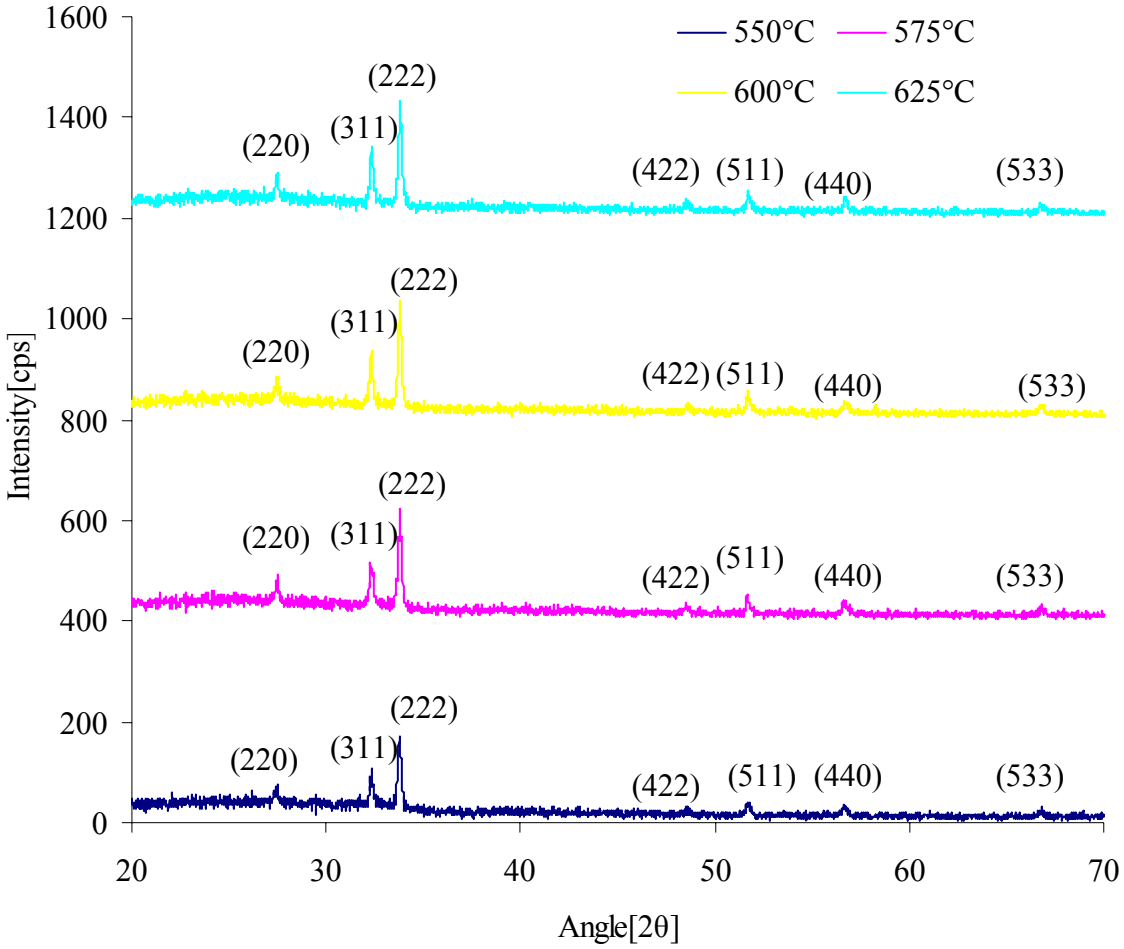

Figure 50. XRD of Cd_2SnO_4 films annealed at four different temperatures

are stable even at high temperatures which is an important parameter in view of the fact that films are subjected to high temperatures in further processing steps. Optical transmission is determined for films of 2500A˚ annealed in He ambient. Figure 51 shows the transmission spectra of Cd_2SnO_4 films annealed at different temperatures. It is evident from the transmission spectra that the Cd_2SnO_4 films annealed at higher temperatures are highly transparent at all wavelengths between 350 and 1000nm. This might be due to the increase in crystallinity of the film as the temperature increases. The average transmission for Cd_2SnO_4 films, between wavelengths of 400 and 1000nm, annealed at

550°C, 575°C, 600°C and 625°C is 88%, 91%, 92% and 93% respectively. The change in resistivity of the films with the annealing temperature is also studied.

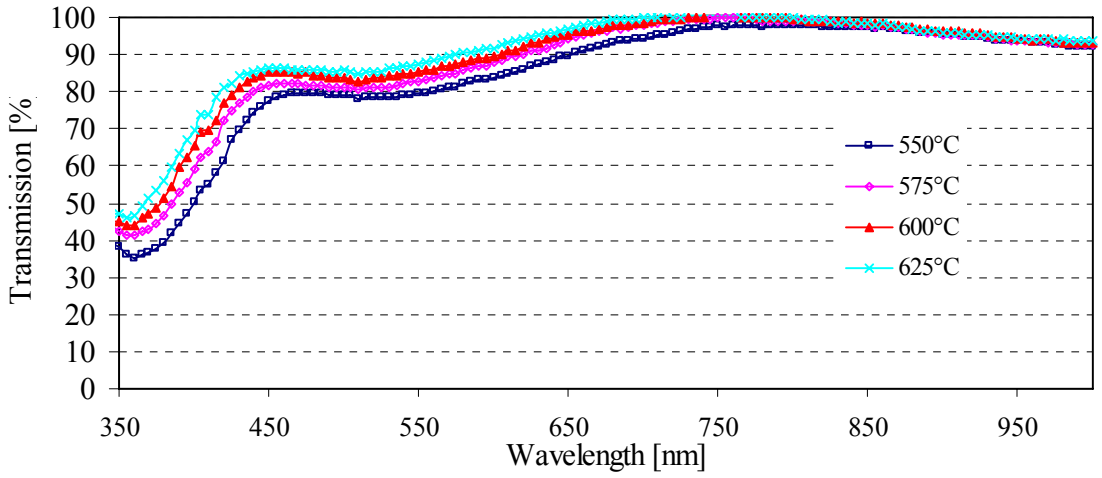

Figure 51. Transmission spectra of Cd_2SnO_4 films annealed at four different temperatures

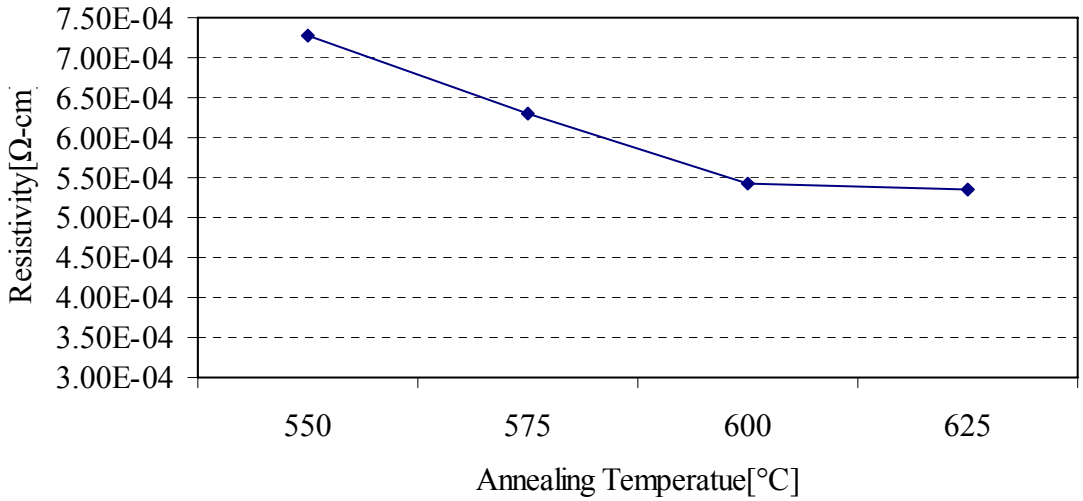

Figure 52. Dependence of resistivity on annealing temperature

Figure 52 shows an improvement in the resistivity of the film as the annealing temperature is increased from 550°C to 625°C. This might be attributed to the improvement in the crystallinity of the film at higher temperatures. As the crystallinity increases, the mobility of carriers also increases thereby increasing the conductivity of the film.

5.4.1.2 Effect of stoichiometry on structural, optical and electrical properties of cadmium stannate film

The effect of stoichiometry on structure, optical and electrical properties of Cd_2SnO_4 is studied by varying the amount of CdO and SnO_2 in the Cd_2SnO_4 film. This is done by controlling the thickness of CdO and SnO_2 materials while sputtering. Figures 53, 54 and 55 show the XRD patterns, transmission spectra and resistivity of the cadmium-rich Cd_2SnO_4 film.

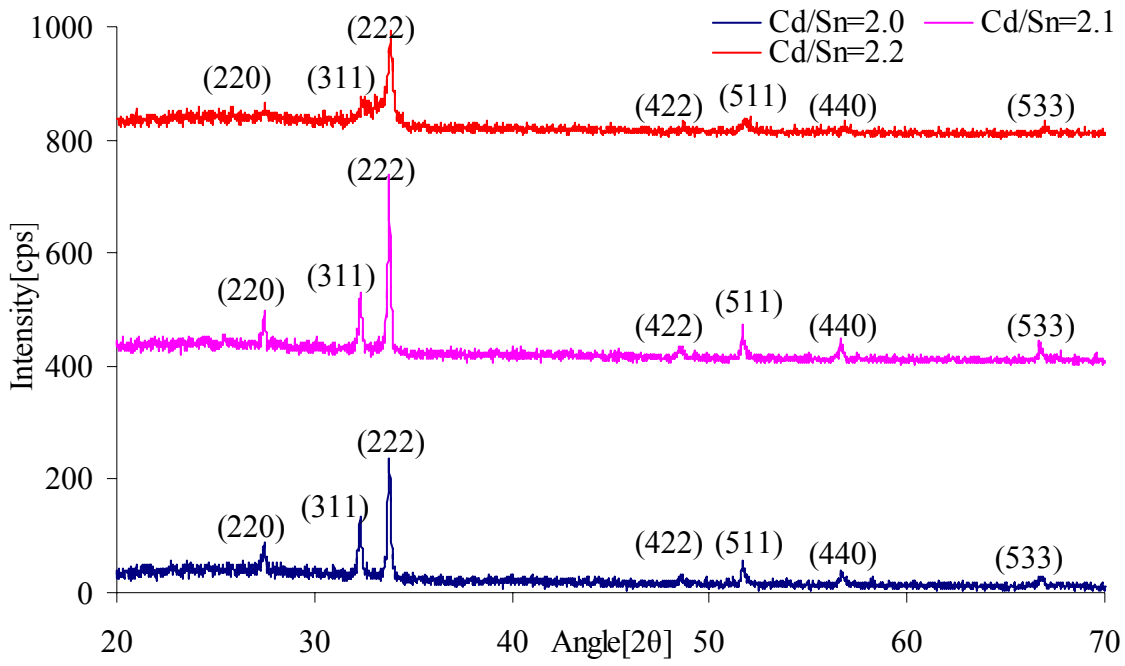

Figure 53. XRD patterns of cadmium stannate films for varying stoichiometry

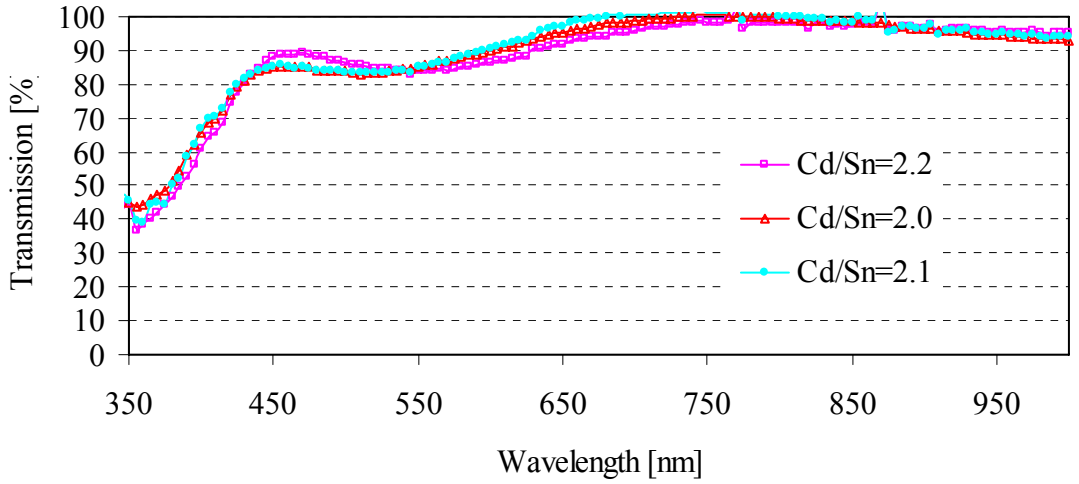

Figure 54. Transmission spectra of cadmium stannate films for varying stoichiometry

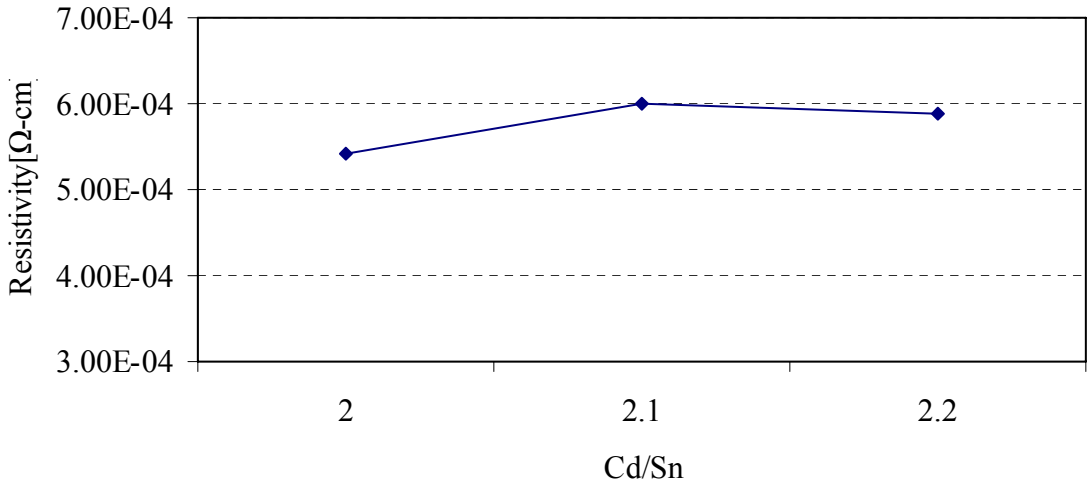

Figure 55. Dependence of resistivity of cadmium stannate films for varying stoichiometry

All the films are deposited at room temperature and annealed at 600°C in He ambient. The XRD patterns of all the films are similar except that the (311) peak of the film with Cd/Sn = 2.2 is starting to emerge. This is because the energy supplied by 600°C annealing is not sufficient to totally crystallize the cadmium stannate film with Cd/Sn =

2.2. All the films show preferred orientation in [222] direction. The average transmission for the films with Cd/Sn=2.0, 2.1 and 2.2 is 92.3%, 93% and 91.5% respectively. Low transmission of Cd_2SnO_4 film with Cd/Sn=2.2 is due to its semi-crystalline nature and it can be improved by annealing it at much higher temperatures. The lowest resistivity obtained in this work is 5.4 X 10^{-4} Ω-cm for the film with Cd/Sn = 2.0.

CHAPTER 6

CONCLUSION

6.1 Investigation of materials

The structural and optical properties of the cadmium stannate and zinc stannate materials are studied. Zinc stannate films deposited at room temperature are amorphous. Subsequent annealing at high temperatures made the films crystalline. This annealing also improved the transmission of the films to a great extent. The films deposited at 400°C turned crystalline. Zinc stannate films deposited at room temperature and elevated temperatures are highly resistive.

The cadmium stannate films deposited at room temperature are amorphous. Annealing the films at high temperatures made them crystalline. The electrical and optical properties of the films improved upon annealing.

6.2 Comparison of devices made with zinc stannate as high resistive buffer layer

The best devices obtained are summarized in table 10 and table 11. The CdTe solar cells made with room temperature deposited zinc stannate films suffered from the effect of shunting which led to low open circuit voltages. The high series resistance in the devices led to decreased fill factors. The effect of stoichiometry of zinc stannate film on CdTe solar cell is studied. The Zn rich films of zinc stannate showed better performance compared to other stoichiometric zinc stannate films. The best devices in this study

Table 14. Summary of the devices with ZTO deposited at room temperature

Zn/Sn	V_{OC}[mV]	FF[%]	J_{SC}[mA/cm^2]	R_{series} [Ω-cm^2]	R_{shunt} [Ω-cm^2]	Efficiency[%]
1.5	710	54.6	24.4	2.32	500	9.45
1.9	770	44.3	24	2.34	730	8.17
2.0	780	58.2	24.5	2.30	800	11.13
2.1	810	66.6	23.1	2.47	800	12.43
2.5	790	66.7	23	1.39	900	12.12

come from the zinc stannate film deposited at elevated temperatures. The devices from these films showed high shunt resistance due to the existence of multiple phases of zinc stannate in the films. This helped in achieving better performance of the devices

Table 15. Summary of the best devices with ZTO deposited at 400°C

ZTO Thickness[Å]	V_{OC}[mV]	FF[%]	J_{SC}[mA/cm^2]	R_{series} [Ω-cm^2]	R_{shunt} [Ω-cm^2]	Efficiency [%]
500	830	69.3	24.74	1.33	1900	14.21
750	830	68.2	24.84	1.75	1900	14.04

REFERENCES

1. H.L.Hartnagel, A.L.Dawar, A.K.Jain, C.Jagadish, "Semiconducting transparent thin films", IOP Publishing ltd, Philadelphia, 1995.

2. Brain G.Lewis, David C.Paine,"Applications and processing of transparent conducting oxides", MRS bulletin, August 2000.

3. David S.Ginley, Clark Bright, "Transparent conducting oxides", MRS bulletin, August 2000.

4. Roy G.Gordon, "Criteria for choosing transparent conductors", MRS bulletin, August 2000.

5. Timothy J.Coutts, David L.Young, Xiaonan Li "Characteization of transparent conducting oxides", MRS bulletin, August 2000.

6. A.J. Freeman, K.R. Poeppelmeier, T.O. Mason, R.P.H. Chang, T.J Marks, "Chemical and thin film strategies for new transparent conducting oxides", MRS bulletin, August 2000.

7. D.R. Kammler, T.O.Mason, "Phase relationships, transparency and conductivity in the cadmium indate-cadmium stannate system", Chem.Mater. 12 (2000) 1954.

8. T.Stapinski, E. Leja, T. Pisarkiewicz, "Point defects and their influence on electrical properties of reactive sputtered Cd_2SnO_4 thin films", J.Phys.D: Appl. Phys. 17 (1984) 407.

9. Y.Dou, R.G. Egdell, "n-type doping in Cd_2SnO_4: A study by EELS and photoemission", Physics Review B. 53 (1996) 23.

10. Timothy J.Coutts, David L.Young, Xiaonan Li, "Search for improved transparent conducting oxides: A fundamental investigation of CdO, Cd_2SnO_4 and Zn_2SnO_4", J.Vac.Sci.Technol.A. 18 (2000) 2646.

11. S. B. Zhanga and Su-Huai Wei, "Self-doping of cadmium stannate in the inverse spinel structure", Applied Physics Letters, 80 (2002) 1376.

12. X.Wu, W.P. Mulligan, T.J. Coutts, "Recent developments in RF sputtered cadmium stannate films", Thin solid films 286 (1996) 274.

13. Timothy J.Coutts, David L.Young, D.L. Williamson, "Structural characterization of zinc stannate thin films", Journal of Applied Physics 91 (2002) 1464.

14. David L. Young, Helio Moutinho, Yanfa Yan, and Timothy J. Coutts, "Growth and characterization of radio frequency magnetron sputter-deposited zinc stannate, Zn_2SnO_4, thin films", Journal of Applied Physics 92 (2002) 310.

15. X.Wu, P. Sheldon, T.J. Coutts, D.H. Rose, H.R. Moutinho, "Application of transparent conducting oxides in CdS/CdTe thin film devices", 26th IEEE PVSC, Sept. 30-Oct.3,1997, p.347.

16. X. Wu, R.G. Dhere, D.S. Albin, T.A. Gessert, C. DeHart, J.C. Keane, A. Duda, T.J. Coutts,S. Asher, D.H. Levi, H.R. Moutinho, Y. Yan, T. Moriarty, S. Johnston, K. Emery, and P. Sheldon, "High-Efficiency CTO/ZTO/CdS/CdTe Polycrystalline Thin-Film Solar Cells", NCPV Program Review Meeting; Lakewood, Colorado, October 14-17, 2001.

17. Timothy J.Coutts, David L.Young, D.L. Williamson, "Structural, optical and electron transport qualities of zinc stannate thin films", Mat.Res.Soc.Symp.Proc. 666 (2001) F3.8.1.

18. R.Mamazza, S.Yu, D.L.Morel, C.S.Ferekides, "Co-sputtered Cd_2SnO_4 films as front contacts for CdTe solar cells", 29th IEEE PVSC, 2002, May 19-24, 2002, p.612.

19. J.E. Granata, J.R. Sites, A.D Compaan "Effect of CdS thickness on CdS/CdTe quantum efficiency", 25th IEEE PVSC, May 13-17, 1996, p.853.

20. X. Wu, S. Asher, D. H. Levi, D. E. King, Y. Yan, T. A. Gessert, and P. Sheldon, "Interdiffusion of CdS and Zn_2SnO_4 layers and its application in CdS/CdTe polycrystalline thin-film solar cells", Journal of Applied Physics, 89 (2001) 4564.

21. X.Wu, W.P. Mulligan, T.J. Coutts, "Properties of transparent conducting oxides formed from CdO and ZnO alloyed with SnO_2 and In_2O_3", J.Vac.Sci.Technol.A. 15(1997) 1057.

22. R.Mamazza, Ph.D. Dissertation, "Ternary Spinel Cd_2SnO_4, $CdIn_2O_4$, and Zn_2SnO_4 and Binary SnO_2 and In_2O_3 Transparent Conducting Oxides as Front Contact Materials for CdS/CdTe Photovoltaic Devices", University of South Florida, 2003.

23. U.Balasubramanian, Masters Thesis, "Indium oxide as a high resistive buffer layer for CdTe/CdS solar cells", University of South Florida, 2004.

24. Alan L. Fahrenbruch, Richard H.Bube, "Fundamentals of solar cells", Academic Press, Newyork 1983.

25. S.O Kasap, “Principles of Electronic materials and devices” Second Edition, Mc Graw Hill, 2002.

26. S.M.Sze, “Physics of semiconductor devices” Second Edition, John Wiley & Sons, Newyork, 1981.

27. Martin A. Green, “Solar Cells: Operating Principles, Technology and System Applications”, Prentice-Hall, New Jersey, 1982.

28. H.J. Moller, “Semiconductors for solar cells”, Artech house, London 1993.